Eruption dynamics at Mount St. Helens imaged from broadband seismic waveforms: Interaction of the shallow magmatic and hydrothermal systems

Gregory P. Waite,[1,2] Bernard A. Chouet,[1] and Phillip B. Dawson[1]

[1] The current eruption at Mount St. Helens is characterized by dome building and shallow, repetitive, long-period (LP) earthquakes. Waveform cross-correlation reveals remarkable similarity for a majority of the earthquakes over periods of several weeks. Stacked spectra of these events display multiple peaks between 0.5 and 2 Hz that are common to most stations. Lower-amplitude very-long-period (VLP) events commonly accompany the LP events. We model the source mechanisms of LP and VLP events in the 0.5–4 s and 8–40 s bands, respectively, using data recorded in July 2005 with a 19-station temporary broadband network. The source mechanism of the LP events includes: 1) a volumetric component modeled as resonance of a gently NNW-dipping, steam-filled crack located directly beneath the actively extruding part of the new dome and within 100 m of the crater floor and 2) a vertical single force attributed to movement of the overlying dome. The VLP source, which also includes volumetric and single-force components, is 250 m deeper and NNW of the LP source, at the SW edge of the 1980s lava dome. The volumetric component points to the compression and expansion of a shallow, magma-filled sill, which is subparallel to the hydrothermal crack imaged at the LP source, coupled with a smaller component of expansion and compression of a dike. The single-force components are due to mass advection in the magma conduit. The location, geometry and timing of the sources suggest the VLP and LP events are caused by perturbations of a common crack system.

1. Introduction

[2] Mount St. Helens began erupting in October 2004 after 18 years of quiescence. Swarms of small (M ≤ 2), shallow (depth ≤ 2 km below the surface) earthquakes marked the onset of renewed activity on 23 September [e.g., *Dzurisin et al.*, 2005; *Moran et al.*, 2008; *Scott et al.*, 2008; *Thelen et al.*, 2008]. Seismic energy generally increased until the first phreatic eruption, which occurred on October 1. Several fluctuations in seismic energy accompanied four more phreatic eruptions through October 5. The period from September 29 through October 5 saw the highest seismic energy release of the eruption [*Dzurisin et al.*, 2005]. On 11 October, a new lava dome emerged from the glacier ice in the south crater. This new dome is erupting as a series of viscous spines that initially grew to the south, with younger, more steeply inclined spines overlying older, flat-lying spines. Dome growth has continued through the present at a relatively steady rate.

[3] The rate of earthquake occurrence settled into a fairly regularly spaced-pattern of small events interrupted by occasional larger (M ≥ 2) earthquakes. These earthquakes are located within the crater near the vent and at shallow depths of less than 2 km below the surface [*Moran et al.*, 2008; *Thelen et al.*, 2008]. Most of the events were occurring in families of similar events that persisted for up to several weeks [*Thelen et al.*, 2008]. By late 2004, the occurrence of these earthquakes became so regular, at approximately 1–3 min intervals, that the term "drumbeat" was used to describe them [*Moran et al.*, 2008]. The event interval increased with time to 3–6 min by July 2005.

[4] There is uncertainty about the origin of these drum-beat earthquakes. In particular, *Iverson et al.* [2006] ascribe them to stick-slip motion between the extruding lava and conduit walls [see also *Iverson*, 2008; *Harrington and Brodsky*, 2007]. A gouge layer 1–2 m thick on the outside of the lava spines [e.g., *Cashman et al.*, 2008; *Pallister et al.*, 2008], the regularity and similarity of the shallow earthquakes, and a fairly regular extrusion rate [e.g., *Schilling et al.*, 2008] seem consistent with a stick-slip model for these earthquakes. However, despite a deliberate effort

---

[1]U.S. Geological Survey, Volcano Hazards, Menlo Park, California, USA.
[2]Now at Geol. & Mining Eng. & Sci., Michigan Technological University, Houghton, Michigan, USA.

to capture stick-slip motions of the spine geodetically, no stick-slip events have been documented (D. Dzurisin, personal communication, 2007). Also, there have been periods during which at least part of the spine had temporarily stopped extruding, but earthquakes continued including one well-documented 4-h-long period (D. Dzurisin, personal communication, 2007).

[5] Our observations, made primarily with a 19-station temporary broadband seismic network, are also inconsistent with a stick-slip or a shear-faulting source. A stick-slip extrusion event could be represented as a combination of a double couple due to shear near the surface, where the viscosity is very high, plus a near-vertical single force (assuming near-vertical spine growth). The relative importance of the shear and single-force components would depend on the coupling between the conduit and the magma. While the onsets of the earthquakes are typically emergent, where they are distinguishable, we observe dilatational first motions on all the broadband stations. Likewise, the short-period network data typically show no clear compressional first motions [see also *Moran et al.*, 2008]. This is inconsistent with a double-couple mechanism, which will produce a mix of compressional and dilatational first motions. If a near-vertical single force dominates the proposed stick-slip mechanism, however, the dilatational first motions could result from the downward reaction force on the Earth due to vertical acceleration of the spine.

[6] Additional information about the source process comes from the stacked frequency spectra of similar events that show energy is concentrated in the band 0.5–2 Hz and spectral peaks are common to multiple stations. These spectral characteristics are indicative of a resonating source, and are not typical of a stick-slip event. The nearly identical waveforms and locations suggest a repetitive, non-destructive source process. Taken together, these observations are inconsistent with a shear-faulting source. This is confirmed by our waveform modeling. We attribute these observations to a volumetric source and refer to the drumbeat earthquakes we analyze as long-period (LP) earthquakes.

[7] LP earthquakes have been widely observed and analyzed at many volcanoes, although they are sometimes called by other names (see *Chouet* [1996a] and *McNutt* [2005] for reviews). Theoretical [e.g., *Ferrazzini and Aki*, 1987; *Chouet*, 1988] and laboratory [e.g., *Burlini et al.*, 2007] studies demonstrate that LP earthquakes are related to the interaction of a fluid and solid, such as resonance in a fluid-filled crack. The compositions of the fluids, the dimensions of the cracks, and the trigger mechanisms are debated, but certainly vary by volcano and even within a single volcano to some degree.

[8] We also observe very-long-period (VLP) events, with periods of 15–25 s, commonly accompanying the LP events. The VLP energy is generally too weak to be detected more than 2 km from the center of the crater, but several larger earthquakes (M > 2.5) have much more associated VLP energy that is observable on stations 6 km from the crater. Because of instrumental limitations, observations of VLP seismicity associated with volcanic activity have been made less frequently than LP observations. Apart from the VLP energy generated by the 18 May 1980 eruption and landslide [*Kanamori and Given*, 1982], VLP signals had not been observed at Mount St. Helens before this study.

[9] Where VLP earthquakes have been observed [*Kawakatsu et al.*, 1992; *Kawakatsu et al.*, 1994; *Neuberg et al.*, 1994; *Kaneshima et al.*, 1996; *Ohminato et al.*, 1998; *Arciniega-Ceballos et al.*, 1999; *Legrand et al.*, 2000; *Nishimura et al.*, 2000; *Rowe et al.*, 2000; *Kumagai et al.*, 2001; *Almendros et al.*, 2002; *Hidayat et al.*, 2002; *Hill et al.*, 2002; *Aster et al.*, 2003; *Chouet et al.*, 2003, 2005] they are typically attributed to fluid-rock interactions, as with LP events. However, instead of resonance in a fluid-filled crack, VLP events may result from longer-term inertial volume changes in fluid conduits. For instance, in analog experiments, a gas slug rising through a liquid-filled tube produces a complex change in the flow of both the gas and liquid falling around it, when it encounters a flare in the tube [*James et al.*, 2006]. This results in, for example, a pressure pulse in the liquid and a downward force on the apparatus holding the tube.

[10] We modeled the source mechanisms of 68 LP earthquakes and five VLP events that occurred between 21 June and 26 July 2005. One event, which had clearly recorded LP and VLP signals, is discussed in detail. We begin with a description of the broadband network and LP and VLP data, and proceed with the inversion and forward modeling methodology. Finally, we provide an interpretation of the crack system that connects the shallow LP and VLP sources.

2. Data

[11] The Pacific Northwest Seismograph Network and U. S. Geological Survey Cascades Volcano Observatory (CVO) operate a network of permanent, telemetered seismographs at Mount St. Helens. Most of these stations are equipped with short-period, vertical-component sensors and use analog telemetry for real-time data transmission. Additional stations have been placed within the crater to help constrain the locations of the shallow earthquakes that are occurring during this eruption. While these stations are well suited to monitoring tasks such as earthquake detection and location, they are not designed to record seismic signals with periods longer than 1 or 2 s. In order to investigate these longer-period signals, we deployed a temporary network of broadband seismographs.

2.1. Broadband Seismic Network

[12] Our data were recorded with an array of 19 three-component broadband seismographs on loan from the Incorporated Research Institutions for Seismology Program for Array Seismic Studies of the Continental Lithosphere instrument center, and a permanent broadband station that is part of the Cascades Volcano Observatory monitoring network (Figure 1). An inner ring of six seismographs was placed on the edifice and breach in the crater wall between 1.2 and 2.3 km from the vent at elevations between 1650 and 2300 m. These six stations were installed with helicopter support. A second ring of seven stations was placed between 1300 and 1600 m elevation at distances of 2.9 to 4.0 km from the vent. Two of the seven stations in the second ring were installed and serviced with helicopter support. The outer ring of seven stations included the permanent broadband station STD on Studebaker Ridge. The elevations of these stations were between 1000 m and
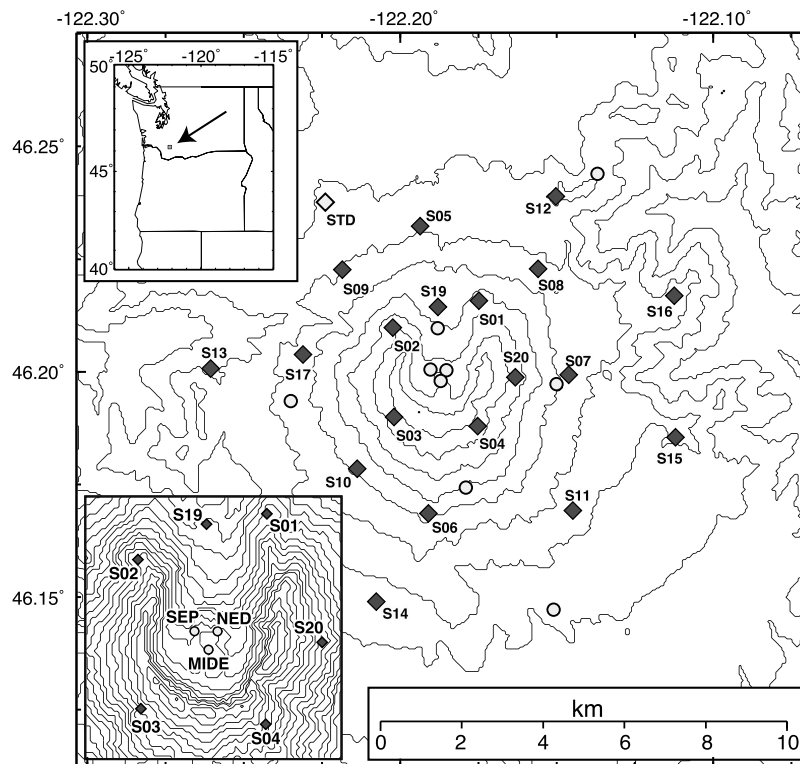
Figure 1. Location map shows the temporary broadband stations (dark diamonds) and a subset of the permanent network stations (light circles and diamond) plotted on topography contoured at 200 m intervals. Station STD was the only permanent broadband station running during the temporary deployment. Inset in the upper left corner shows the location of Mount St. Helens in southern Washington State. Inset in the lower left corner shows a close-up of the crater stations MIDE, NED, and SEP discussed in the text, with 40 m topographic contours.

1400 m at distances of 4.6 to 6.3 km from the vent. Station S16 was the only outer ring station that was installed and serviced by helicopter. The remaining stations were installed by small teams who packed the equipment to the sites on foot.

[13] Eighteen of the sites were equipped with three-component Güralp CMG 40T sensors (0.02–30 s) and Reftek 130 digitizer-recorders. One station had a three-component Streckeisen STS-2 (0.02–120 s) and Reftek 130 digitizer-recorder (station S19), and the permanent station STD has a three-component Güralp CMG-6TD sensor (0.02–30 s) with integrated digitizer and recorder. All data loggers used Global Positioning System (GPS) timing. The data from STD were digitally telemetered in real time to CVO at 50 samples per second. The 19 temporary stations recorded data at 100 samples per second on site to two 2 Gb flash memory cards that required downloading approximately every 4 months.

[14] The locations of the sensors were determined with Wide Area Augmentation System-enabled GPS for accuracy of 2–5 m. The horizontal components were oriented with a compass. We examined surface wave polarizations to confirm the accuracy of the sensor orientations and found two stations, S03 and S08, with orientations that vary by more than 5°. These data were corrected during processing.

[15] While most of the stations performed well during the deployment, there were various problems with the six closest stations (S01, S02, S03, S04, S19, S20). For consistency in the analysis, we address a single time period from 21 June through 26 July during which stations S01, S02, S03, and S04 were all functioning properly.

2.2. LP Data

[16] By summer 2005, when the broadband network was installed, the seismic activity had settled into a pattern of LP seismicity occurring at fairly regular intervals of several minutes. We describe the key characteristics of these events below.

2.2.1. Waveform Similarity

[17] Waveforms for the majority of the LP events are remarkably similar when viewed in the LP band [see also *Thelen et al.*, 2008]. We quantified the waveform similarity using waveform cross-correlation. We began by running an amplitude and signal-to-noise-based triggering algorithm over all the data at station S11 after filtering between 1–4 s. This station was chosen because it had the longest record of continuous recording of the stations in the temporary network. We then computed the cross-correlation coefficient between triggered events over a 13 s window that included 5 s of pre-trigger noise. We began with the first trigger in the catalog and computed cross-correlation coefficients for all subsequent triggers (Figure 2). Between 17 June and 8 September 2005 we found 40%, or 5394 of the 13,604 events detected at station S11 correlated with the very first event detected at a correlation coefficient of at least 0.90. Over that same period, 64% correlated at 0.80 or
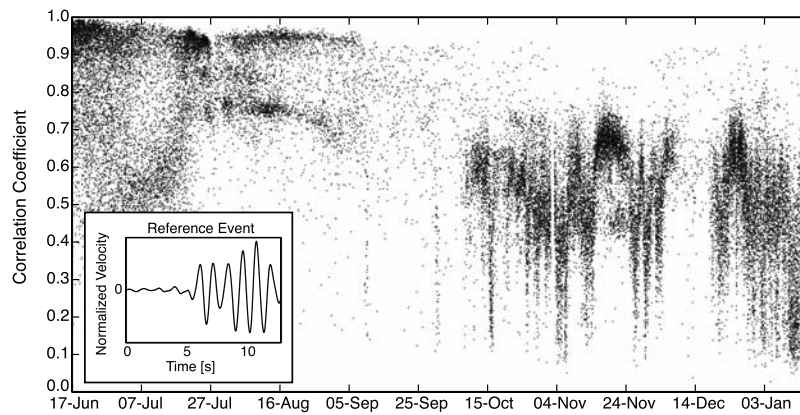
Figure 2. Correlation coefficients of all the triggered events recorded during the temporary deployment with respect to the first trigger. The cross-correlation was determined using station S11, because it was the most consistent station during the deployment, and the reference event, which is shown in the inset. The majority of the events recorded between 17 June and 8 September correlate above 0.8. Forty percent of the events during that time correlate at 0.9 or above.

above and 92% correlated at 0.60 or above. The similarity gradually degraded with time; after 8 September, there are no events that correlate with the reference event at a correlation coefficient of 0.95 or above. When we selected a reference event that occurs later in the recording period, we typically saw a gradual increase and decrease in waveform similarity before and after the event, similar to the observations of *Thelen et al.* [2008] made during late 2004.

[18] When examined at stations closer to the vent, the waveforms show subtle changes with time. For example, Figure 3 shows records from station S02 of all the events in July 2005 with a cross-correlation coefficient of 0.95 or higher, as measured at station S11. The waveforms are aligned based on the maximum cross-correlation measured at S11. The broadband waveforms for events from 1–12 July are similar, but there is a change in the source that occurs between 12 and 18 July. The last 12 days of July again have very similar waveforms, but include additional shorter-period components (this change was also discussed by *Moran et al.* [2008]). This may reflect a change in the spatial or temporal properties of the triggering excitation of the source while the geometry of the resonator remains unchanged. For example, a variation in the location of the trigger of a resonating crack could induce stronger resonance in higher modes [e.g., *Chouet*, 1992; *Kumagai et al.*, 2002]. The change is also related to a westward shift in the best fit point source locations of the modeled LP earthquakes, which is discussed below.

2.2.2. First Motions

[19] The first motions of the LP events are typically emergent, but where they are distinguishable, first motions are dilatational on all the broadband stations. Figure 4 shows vertical velocity waveforms for a M_C 3.3 event that occurred at 9:34:39 on 31 July 2005, which produced dilatational arrivals on all of the broadband stations. Even station LON (not shown in Figure 4), which is 67 km NE of the source, has a clear dilatational first motion. The larger events are not similar to the LP earthquakes in general [see also *Moran et al.*, 2008], but this particular earthquake correlates with our reference event at a correlation coefficient of 0.90.

[20] A dilatational first motion on all stations may indicate a source with a net volume decrease, such as collapse of a crack, or a source dominated by a near-vertical single force. Alternatively, a CLVD mechanism might fit the dilatational broadband observations, as indicated in the inset of Figure 4, if there is a small region of compressional arrivals in the center of the focal sphere. For example, *Nettles and Ekström* [1998] modeled a complex CLVD mechanism having an elliptical region of compression surrounded by dilatation as thrust faulting on an outward-dipping, cone-shaped fault system. However, this mechanism calls for motion opposite to what we would expect for upward motion of a magma plug. When we include the short-period network observations, which are also all dilatational for this event, we see there is little room for a compressional region in the focal mechanism. *Aki* [1984] demonstrated the difficulty in constraining magma-intrusion-related CLVD mechanisms with first motions alone, owing to the difference in period expected for different components of the ground response to the sudden
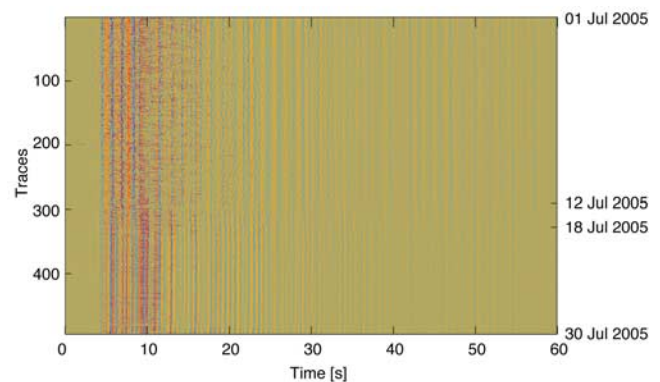

Figure 3. Waveforms of 493 similar events recorded at station S02 in July 2005. The waveforms are aligned based on the cross-correlations determined at station S11; events with correlation coefficients of 0.95 and above are plotted (see Figure 2). Notice the change in waveform character that occurs between 12 and 18 July.
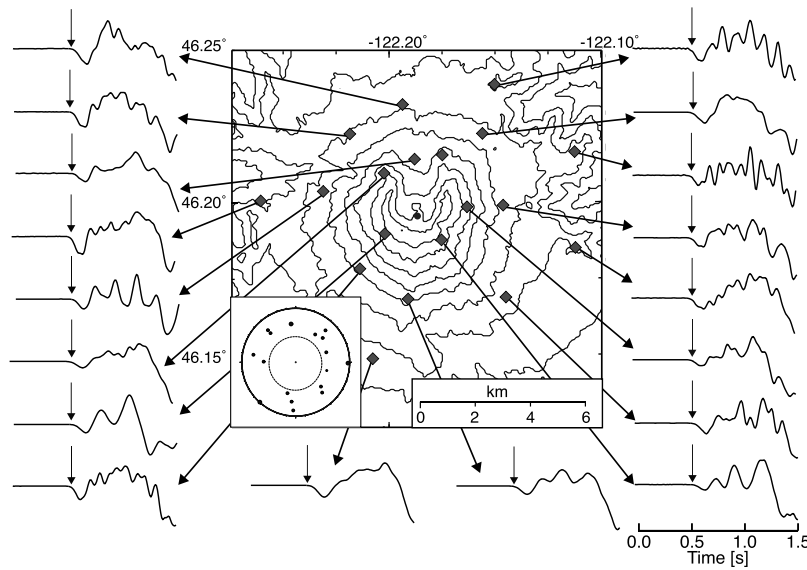
Figure 4. Dilatational first motions are clear at all of the broadband stations for a sample event from 31 July 2005, plotted as a circle in the crater. The focal sphere in the inset shows distribution of the first motion recordings for the broadband stations, with a dashed line in the middle outlining the region where there are no broadband stations.

opening of a tensile crack [see Figure 4 in *Chouet*, 1981]. So, while the first motions suggest a volumetric source, waveform modeling is required to clearly identify it.

2.2.3. Frequency Spectra

[21] Records of individual earthquakes recorded on the closest short-period stations (e.g., SEP) have frequencies up to 30 Hz, although the highest spectral peaks are below 10 Hz. The high frequencies are absent in the broadband records of even the closest stations, ~1.2 km from the center of the crater, indicating a highly attenuating medium [e.g., *Thelen et al.*, 2007]. The lower frequencies (<3 Hz) that are observed in the broadband data are clearly seen on the closest short-period stations. Figure 5 shows examples of two earthquakes that occurred 435 s apart on 22 July 2005, along with the frequency spectrum of each event. These earthquakes have similar amplitudes and durations,
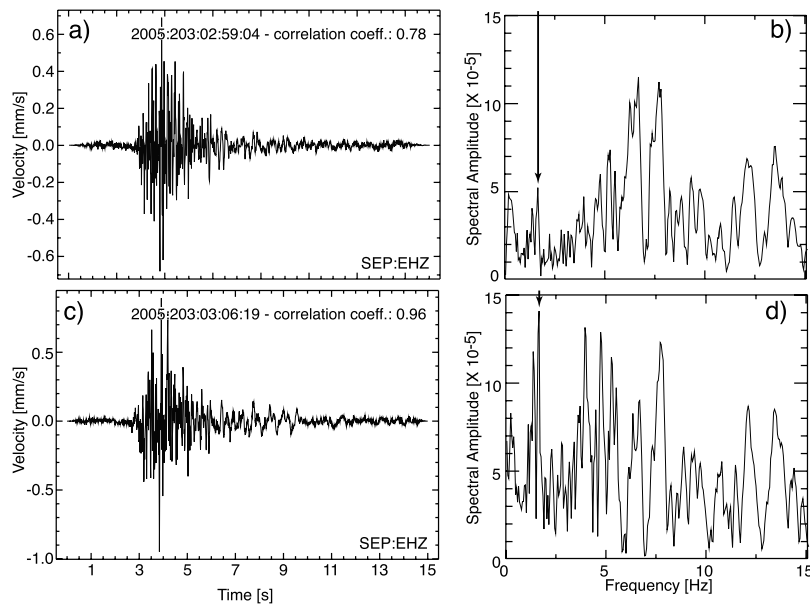

Figure 5. Two consecutive (435 s apart) drumbeat earthquakes recorded at the closest short-period velocity sensor used to illustrate the difference between events with high and moderate cross-correlation coefficients (as measured at S11, see Figure 2). The second event has significantly more low-frequency energy, which is evident in the waveform (c) and spectrum (d). This spectral peak, which is marked by an arrow at 1.7 Hz, is also evident in the earlier event, but it does not dominate the spectrum (b) and it is difficult to see in the waveform (a). The 1.7 Hz peak is observed on all the stations for the similar events.
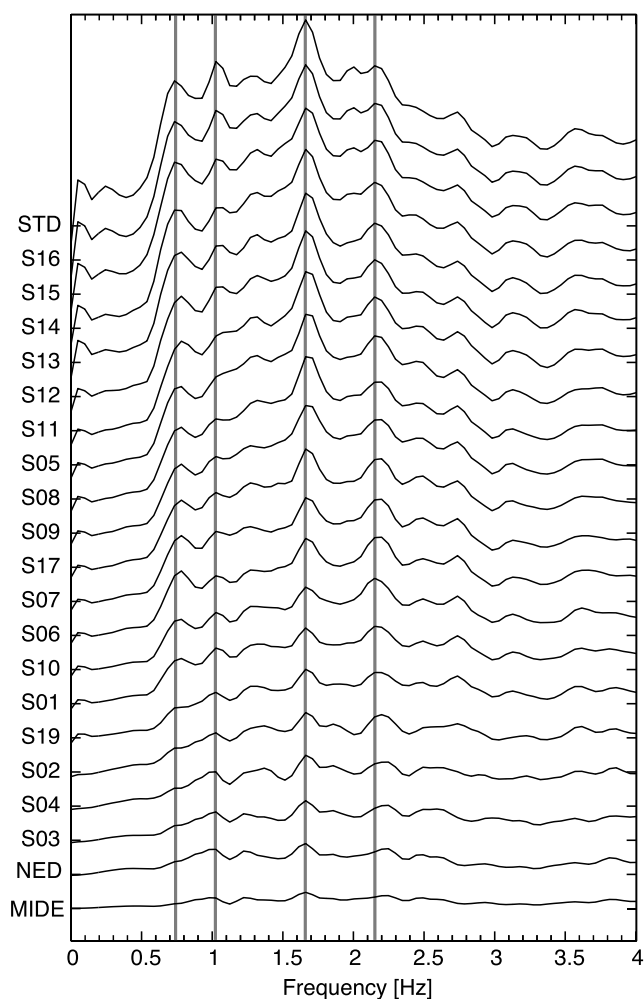
Figure 6. Stacked spectra from 19 similar events recorded on 22 July 2005. Epicentral distance increases from bottom to top. The spectrum for each station is the sum of the spectra of all the stations below it (closer to the epicenter). The instrument responses were deconvolved from the accelerometer data from MIDE and NED before the Fourier transform to frequency was applied.

but clearly have different waveforms. The later event (plotted in Figure 5c) has a much stronger low-frequency signal that is evident in the waveform as well as the frequency spectrum (Figure 5d). The peak energy for this event is at about 1.7 Hz (see arrow in Figure 5d). The 1.7 Hz peak is also evident in the earlier event (see arrow in Figure 5b), but there is more energy in the higher frequencies from 5–8 Hz. The correlation coefficients of each of these events and the reference event determined at station S11 as described above, are printed above each waveform. The event with peak energy at 1.7 Hz is very similar to the reference event, having a correlation coefficient of 0.96.

[22] Stacked frequency spectra from similar events suggest that the 1.7 Hz peak is a dominant frequency of the source process. Figure 6 shows the stacked spectra from vertical velocities of 19 similar (cross-correlation coefficient ≥0.95) events recorded on 22 July 2005. Beginning at the bottom are accelerometer stations MIDE and NED, which are closest to the source, followed by broadband stations at increasing epicentral distances. The accelerometer data were integrated to velocity, after deconvolving the instrument responses, before the Fourier transform to frequency was applied. Station SEP, discussed previously, was not used because the data it recorded are clipped for many of the earthquakes. In order to demonstrate the similarity of spectral peaks at multiple stations, the individual stacks were combined with increasing epicentral distance. For example, the line marked NED is the sum of stacked spectra from both MIDE and NED; the third line from the bottom is the sum of stacked spectra from MIDE, NED and S03; and so on. This stacking has the effect of highlighting the most consistent peaks. Clearly the 1.7 Hz peak dominates, with subdominant peaks at 0.7, 1.0, and 2.1 Hz. Also, there is relatively little energy above 2.5 or 3 Hz.

2.3. VLP Data

[23] The two broadband stations nearest to the vent, S03 and S04, recorded VLP signals accompanying many of the LP earthquakes. In fact, there is a one-to-one correspondence of VLP to LP during some time periods (Figure 7). Clear VLP signals are occasionally observed without an
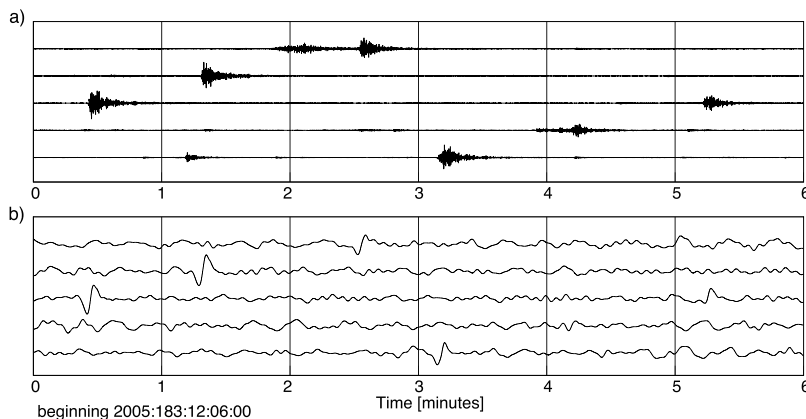
Figure 7. A 30 min record from S03, radial channel, showing the regularly spaced drumbeat earthquakes, which occur about every 5 min, and the VLP pulses that underlie the events. The waveforms in Figure 7a are unfiltered; the waveforms in Figure 7b are bandpass filtered between 30–6 s using a zero-phase-shift, two-pole Butterworth filter. This filter band is slightly different from that used in the modeling, but shows the VLP signals in this record most clearly.
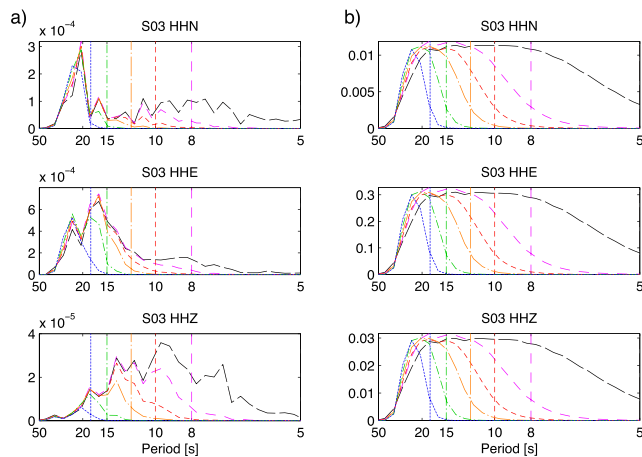
Figure 8. Power spectra of bandpassed signals for two events recorded at station S03. The lower corner of the filters is fixed at 30 s, the upper corner varies: 5, 8, 10, 12, 15, and 18 s. The colored, patterned vertical lines correspond to the upper corner used on the filter for spectra plotted with the same color and pattern. Notice the consistent peaks in the plots in Figure 8a at around 20 s, compared with the plots in Figure 8b, which are highly filter dependent. The VLP peaks in Figure 8a are not affected by the filter until the upper corner is lowered to 15 s.

associated LP and can be seen in the raw velocity records. The horizontal components record larger amplitude VLP signals, but typically record more noise in the VLP band. This makes identifying low-amplitude VLP events difficult. The VLP energy is generally too weak to be detected beyond the closest stations, but several larger earthquakes (M > 2.5) have much more associated VLP energy that is observable on stations up to 6 km from the crater. As with the LP data, similarity among VLP waveforms from different events reflects the repetitive action of a non-destructive source.

[24] We identify VLP waveforms by filtering the data with a band-pass, two-pole, zero-phase-shift, Butterworth filter between 40 and 8 s. Several bands were examined between 50 and 5 s to identify the range that permits the most VLP energy to pass through without allowing additional noise. The lower corner of the CMG-40T sensors we used is 30 s, which is ~3 dB below the flat part of the amplitude response curve. The amplitude response drops another 3 dB at 40 s, which represents a factor of 2 drop in the amplitude response at 40 s from the flat part of the curve. It is therefore reasonable to expect to record signals with periods of up to 40 s. Given the benefit of an increase in the filter width for recovering real signal, the small increase in noise below the 30 s corner of the instrument is acceptable.

[25] Microseismic noise, which overwhelms much of the VLP signal, limited the upper end of the period band we used. Figure 8 demonstrates the effect that changing the high corner has on the filtered signal. In this example we fixed the lower corner at 30 s and varied the upper corner of the filter from 18 to 5 s. The dominant VLP peaks on the horizontal channels are stable for filter corners from 5 s to 12 s for the event shown in Figure 8a. The event in Figure 8b shows a

strong dependence on the filter corner with no clear VLP peaks in the period bands considered. Events such as the event in Figure 8b were not modeled or interpreted as VLP earthquakes. In the cases where the VLP signal was not strongly filter dependent, we found a corner of 8 seconds captured the VLP energy without including significant microseismic noise.

[26] A M_C 3.1 earthquake that occurred on 2 July 2005 had a particularly large associated VLP signal. VLP energy was observed on all the stations in the network that were operating at the time. This event had the clearest VLP signals observable on the most stations, so it was selected for further analysis. Unfortunately, station S20 on the east flank of the volcano did not record this earthquake. Particle velocities are elliptical or rectilinear and point to a VLP source near the center of the crater (Figure 9) and very shallow. However, topography has a strong effect on the waveforms, so particle motion directions alone cannot resolve the source location [e.g., *Ohminato and Chouet*, 1997; *Neuberg and Pointer*, 2000].

[27] Figure 10 shows the broadband and bandpassed velocity and displacement records of the 2 July event from stations S03 and S04. The VLP signal can be seen in the broadband displacement (Figure 10b), but the higher-frequency signals have larger amplitudes. The broadband signal lasts at least 40 s, although there is an indication, especially from the displacement records, that the signal may have a period of 60 s or more. This suggests that the period of the VLP signal may be longer than our 30-s instruments can faithfully record.

3. Data Analysis and Results

[28] We perform full-waveform inversion of the LP and VLP events in a manner similar to the method employed by *Chouet et al.* [2005]. A modification to perform the inversion in the frequency domain [*Auger et al.*, 2006] greatly reduces computation time and permits a grid search over a
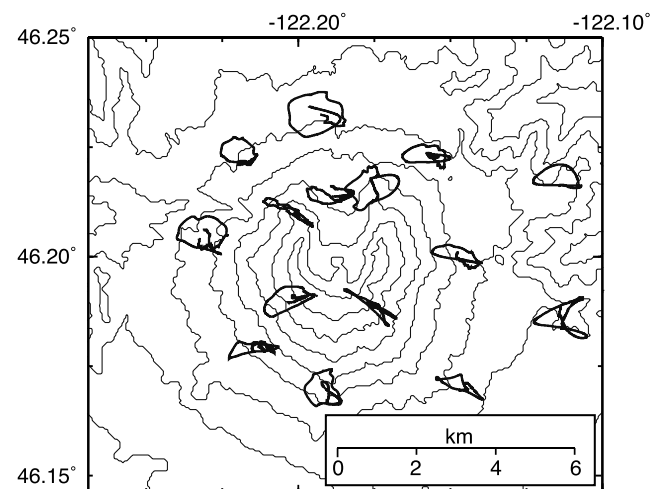

Figure 9. Horizontal particle velocities for the large VLP event on 2 July 2005 are plotted on a station map. Velocities are normalized by station. The outer stations have some noise, but the closest stations have elliptical or rectilinear particle motions that generally point to the vent.
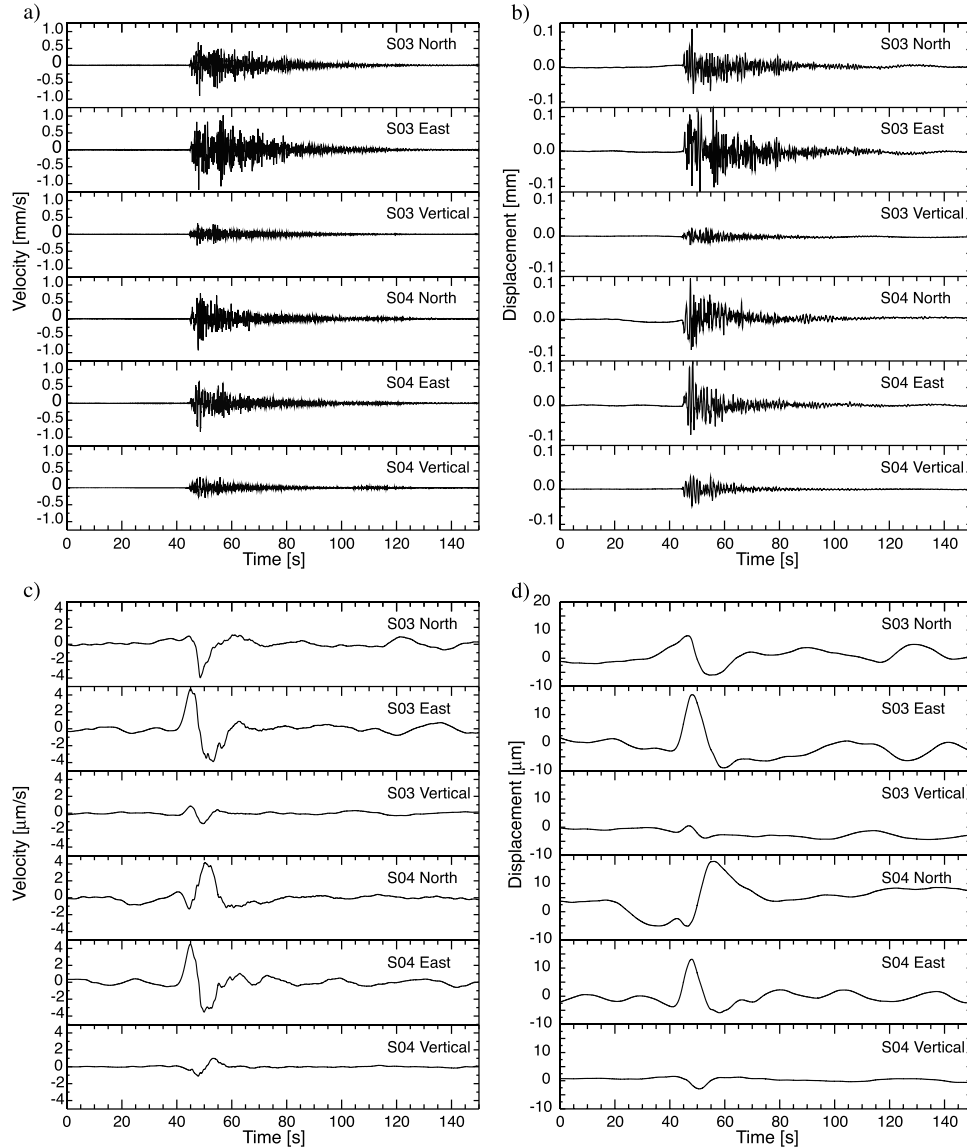
Figure 10. Broadband velocity (a), and displacement (b) records of the 2 July event recorded at the two nearest stations. The VLP signal is clear in the displacement records, but difficult to see in the velocity records. The bandpass-filtered (8–40 s, zero-phase-shift, two-pole Butterworth filter) velocity (c) and displacement records (d) are a factor of 250 and 8 smaller than the broadband records, respectively.

large volume. The inversion method, computations of Green functions, and evaluation of the results are described below.

3.1. Inversion Method

[29] We use the representation theorem to describe the displacement field generated by a point source, which may be written as [*Chouet*, 1996b, equation 8]

$$u_n(\vec{r}, t) = F_p(t) * G_{np}(\vec{r}, t) + M_{pq}(t) * G_{np,q}(\vec{r}, t),$$
$$p, q = x, y, z,$$
(1)

where $u_n(\vec{r}, t)$ is the n-component of the displacement at time t and receiver position $\vec{r}$, $F_p(t)$ is the time history of the force applied in the p-direction, $M_{pq}(t)$ is the time history of the pq-component of the moment tensor, and $G_{np}(\vec{r}, t)$ is the tensor of Green functions that relates the n-component of displacement at the receiver position, $\vec{r}$, with the

p-component of impulsive force at the source position. Although it is not specified in equation (1), $G_{np}(\vec{r}, t)$ depends on the source position as well. The notation $,q$ indicates spatial differentiation with respect to the q-coordinate and the symbol * denotes convolution. Summation over repeated indices is implied.

[30] The frequency domain version of equation (1) is:

$$u_n(\vec{r}, \omega) = F_p(\omega) \cdot G_{np}(\vec{r}, \omega) + M_{pq}(\omega) \cdot G_{np,q}(\vec{r}, \omega),$$
(2)

which we can recast in matrix form as:

$$\mathbf{U}(\omega) = \mathbf{G}(\omega)\mathbf{s}(\omega),$$
(3)

where $\mathbf{U}$ is the $N_\tau \times 1$ vector of Fourier-transformed ground displacement components, $\mathbf{G}$ is the $N_\tau \times 9$ matrix of Fourier transforms of the Green functions, $\mathbf{s}$ is the 9×1 vector of

Fourier transformed force and moment-tensor components, and N_τ is the number of observed seismic traces. We invert at each frequency separately by minimizing the least squares problem and arrive at estimates for the source:

$$\mathbf{s}^s(\omega) = \left[\mathbf{G}(\omega)^H \mathbf{G}(\omega)\right]^{-1} \mathbf{G}^H(\omega)\mathbf{U}(\omega), \qquad (4)$$

where the symbol ^{H} indicates the conjugate transpose (Hermitian) and $\mathbf{s}^s$ is the vector of calculated Fourier transformed source components. After solving for all frequencies of interest, we obtain the time domain estimates of the single-force and moment-tensor components of the source with the inverse Fourier transforms of the relevant components of the vectors $\mathbf{s}^s$. Synthetic seismograms for all the traces are computed in the frequency domain using equation (2) followed by application of the inverse Fourier transform.

[31] Working in the frequency domain reduces the computation time by permitting inversions of many small matrices, which is more efficient than inverting one large matrix [*Auger et al.*, 2006]. It also reduces the number of samples, N_s, so that it is permissible to rapidly compute inversions for traces with on the order of 10,000 time samples. For a trace of 164 s sampled at 50 samples per second, we get 164 samples per Hz. In the case of the VLP data inversions, where we use a limited frequency band from 0.025 to 0.125 Hz, we are effectively inverting with just 16 samples and can loop over a small number of frequencies in the inversion. Our tests demonstrate that results of time domain inversions are not significantly different from frequency domain inversion results.

3.2. Calculation of Green Functions

[32] We compute synthetic Green functions with the three-dimensional (3D) finite-difference method of *Ohminato and Chouet* [1997] using a medium that includes the 3D topography of Mount St. Helens. VLP signals with periods from 8–40 s have wavelengths that range from about 16 to 150 km, so small-scale velocity heterogeneities are assumed to have a negligible effect on the data. For the LP band we use periods from 0.5–4 s; wavelengths are as short as 1 km for the shortest-period shear waves. Since we analyze data from stations up to 4 km away, km-scale heterogeneities may be important.

[33] We compare Green functions calculated using a homogeneous model with those computed using a smooth 3D velocity and density model. In the homogeneous model, we use a *P* wave speed of 3.5 km/s, *S* wave speed of 2 km/s and a density of 2650 kg/m³. The 3D model is based on a local earthquake V_P tomography study that combined network data with the temporary broadband array data [*Waite and Moran*, 2006]. This model is characterized by lower velocities in the volcanic edifice and near the surface than the homogeneous model, but has a fairly simple structure in the shallow subsurface. The *S* wave speed is fixed at $V_P/\sqrt{3}$. Density ρ is calculated following the empirical relation defined by *Onizawa et al.* [2002]:

$$V_P = 6.86 - 7.55\rho + 2.64\rho^2. \qquad (5)$$

We do not find significant differences in the source time functions computed with the 3D and homogeneous models, although in the LP band, the point source locations determined using the homogeneous model are 50–150 m north of, and up to 200 m deeper than those computed with the 3-D model.

[34] We convolve the Green functions with a cosine function to ensure a stable inversion:

$$S(t) = \begin{cases} \frac{1}{2}\left[1 - \cos\left(\frac{2\pi t}{t_p}\right)\right], & 0 \le t \le t_p \\ 0, & t > t_p \end{cases} \qquad (6)$$

where t_p = 0.5 s or 0.25 s depending on the grid spacing (discussed below). The Green functions, convolved with this cosine function, represent the elementary source-time functions used in the inversion. Note that with $t_p = 0.5$ s, the cosine function has frequencies from 0 to 4 Hz.

[35] The model parameterization for the finite-difference calculations represents a compromise between synthetic waveform precision and computational cost. For the VLP band, we can use wider grid spacing, larger t_p, and a model with larger dimensions than we use for the shorter-period LP band. The VLP model domain is centered on Mount St. Helens and has lateral dimensions of 18 km by 18 km and a vertical extent of 10 km. This yields a model with 361 by 361 by 201 nodes spaced 50 m apart. We used $t_p = 0.5$ s to compute the Green functions for the VLP inversions. This node spacing is small enough to satisfy the criterion of minimum number of grids per wavelength of 25 established by *Ohminato and Chouet* [1997] and the number of grid nodes is small enough to allow the computation of Green functions in a reasonable amount of time. At the same time, the model domain is large enough to minimize edge reflections for sources within a few km of the crater floor while including all of the stations.

[36] The shorter periods of the LP data require a finer grid spacing of 20 m to conservatively model wavelengths as short as 1000 m. This finer model has 437 by 437 by 291 nodes and lateral dimensions 8720 by 8720 m and a vertical extent of 5800 m. The Green functions are computed using $t_p = 0.25$ s. This model domain is not large enough to include the entire broadband network, so we only compute Green functions for the 12 closest stations.

[37] The topography data are derived from the combination of two models. The area outside the crater was digitized from U.S. Geological Survey topographic maps. Erosion of the crater rim, the growth of a glacier, and the new lava dome have changed the topography of the crater dramatically since the data for these maps were collected in 1980. We updated that model with new data from photographs taken on 19 April 2005 by *Schilling et al.* [2008]. The top of the model is set to coincide with the highest point on the crater rim at 2550 m.

[38] To determine the best location for a single point source, we conduct a grid search over a volume 1100 m × 1100 m × 1100 m. The volume covers the upper kilometer of the crater floor and includes both the southern part of the crater where the dome building is occurring and the dome created during the 1980–1986 eruption period where, presumably, the conduit that supplied the 1980s lava meets the crater floor.

[39] As an example, at 50 m grid spacing, the number of possible point source locations is 12,167 so 109,503 Green functions are required for the inversions. This represents more than 1,000 days of computation time if each Green function is computed with finite difference individually. Following *Chouet et al.* [2005], we make use of the reciprocity relation to greatly reduce the number of calculations required to derive the Green functions. The reciprocal relation between a source and receiver is described by

$$G_{mn}(\mathbf{x}_1, \mathbf{x}_2) = G_{nm}(\mathbf{x}_2, \mathbf{x}_1), \qquad (7)$$

[*Aki and Richards*, 1980]. This relation states that the *m* component of displacement at $\mathbf{x}_1$ due to a unit impulse applied in the *n* direction at $\mathbf{x}_2$, shown as $G_{mn}(\mathbf{x}_1, \mathbf{x}_2)$ in equation (7), is the same as the *n* component of displacement at $\mathbf{x}_2$ due to a unit impulse applied in the *m* direction at $\mathbf{x}_1$ ($G_{nm}(\mathbf{x}_2, \mathbf{x}_1)$ in equation (7)). Using reciprocity, we calculate the three components of displacement at each source node generated by impulsive forces applied in the *x*, *y*, and *z* directions at each receiver location in the network. The Green functions of the moment components are then derived by spatial differentiation of the results obtained for the forces. For 20 three-component stations, just 60 finite difference runs are required to generate the Green functions for all the point sources, resulting in a dramatic reduction in computation time.

[40] We validate the reciprocity assumption by comparing Green functions computed from source to receiver at several stations with Green functions computed from receiver to source. There are only minor differences in amplitude and phase in the later portions of the time series that result from weak reflections from the model boundaries. *Ohminato and Chouet* [1997] employ approximate absorbing boundary conditions that permit reflection of non-zero incidence plane waves. We could delay and reduce these reflections by enlarging the model or adapting more sophisticated absorbing boundary conditions, but that would significantly increase the time necessary for the finite difference computations. So, while this approximation results in minor differences between the forward and reciprocal Green functions, the discrepancies have insignificant effects on the results of our waveform inversions.

3.3. Evaluation of the Results

[41] We initially consider three possible source mechanisms: (1) three single-force components only; (2) six moment-tensor components only; and (3) six moment-tensor components plus three single-force components. The selection of the most likely mechanism is based on the squared error, the relevance of the free parameters used in the model, and the physical significance of the resulting source mechanism. We use two measures of squared error to evaluate the waveform fits in the time domain [*Ohminato et al.*, 1998; *Chouet et al.*, 2003]

$$E_1 = \frac{\sum\limits_{n=1}^{N_r} \sum\limits_{p=1}^{N_s} \left(u_n^0(p\Delta t) - u_n^s(p\Delta t) \right)^2}{\sum\limits_{n=1}^{N_r} \sum\limits_{p=1}^{N_s} \left(u_n^0(p\Delta t) \right)^2}, \qquad (8)$$

and

$$E_2 = \frac{1}{N_r} \sum\limits_{n=1}^{N_r} \left[\frac{\sum\limits_{1}^{3} \sum\limits_{p=1}^{N_s} \left(u_n^0(p\Delta t) - u_n^s(p\Delta t) \right)^2}{\sum\limits_{1}^{3} \sum\limits_{p=1}^{N_s} \left(u_n^0(p\Delta t) \right)^2} \right], \qquad (9)$$

where $u_n^0(p\Delta t)$ is the *p*th sample of the *n*th data trace, $u_n^s(p\Delta t)$ is the *p*th sample of the *n*th synthetic trace, N_τ is the number of data traces, N_s is the number of samples in each trace, and N_r is the number of three-component receivers. In equation (8), the large amplitude signals on the near-source stations dominate the error so that mismatches between low amplitude data and synthetics do not contribute significantly. In equation (9), the squared error is normalized by station, so that stations with lower amplitude signals contribute to the error equally. We prefer E_2 because it accounts for stations from all distances equally, but we list the E_1 residuals throughout the paper for comparison.

[42] The significance of the number of free parameters is evaluated by calculating Akaike's information criterion (AIC) [*Akaike*, 1974], which is defined as

$$AIC = N_\tau N_s \ln E + 2 N_m N_f, \qquad (10)$$

where *E* is the squared error defined by equation (8) or (9), N_m is the number of source mechanism components, and N_f is the number of frequencies. In general, we can fit the data better with all nine parameters (six moment components and three single forces). The use of a larger number of free parameters is justified if both the squared error and AIC are minimized.

3.4. Results

[43] In the following discussion, we detail the source process of the $M_C 3.1$ earthquake that occurred at 13:29:50 on 2 July 2005. We examine the LP band first, followed by the VLP band. Our analyses of other LP events, including small (M < 2) events, and stacks of LP events follow the detailed evaluation of the 2 July event. All of the similar (i.e., cross-correlation coefficient ≥ 0.9) LP events produce a similar mechanism regardless of whether the first-motions are clearly dilatational or emergent. We chose to describe inversion and the mechanism of the larger 2 July event below because it has a clear VLP signal along with the clear LP signal. We briefly describe the modeling of additional VLP events in section 3.4.3.

3.4.1. LP Band

[44] We modeled 23 channels from the 8 stations that are within 3.5 km of the vent in the band 0.5–4 s. Stations nearer to the edge of the model were not used because of weak reflection artifacts at the model edge. A defective horizontal channel on station S10 was unusable. The best fit location is found directly beneath the growing lava dome at 2000 m above sea level, corresponding to about the elevation of the floor of the 1980 eruption crater (Figure 11). During mid July 2005 the lava dome reached an elevation of 2368 m [*Schilling et al.*, 2008], so its apex was ~350 m above the LP source.

[45] The best fit model, based on residual error E_2 and using six moment-tensor components plus three single-force
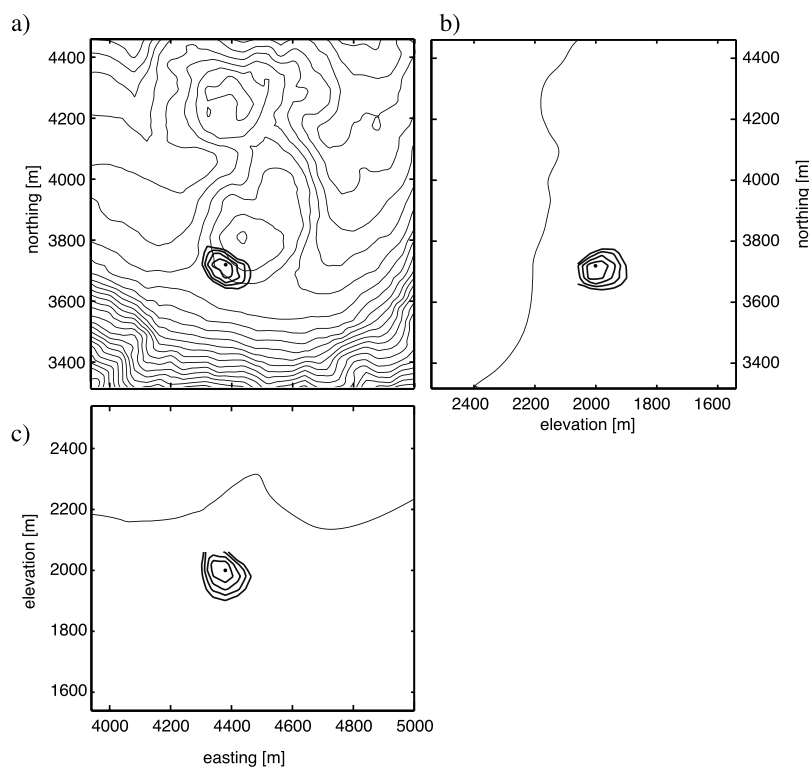
Figure 11. Location of the point source (solid dot) yielding the minimum residual for the 2 July 2005 LP event. A map view (a), and north-south (b) and east-west (c) cross-sections through the minimum residual point are shown. Thin lines in Figure 11a show topographic contours (20 m spacing) within the crater as of April 2005. Heavy lines in all three parts contour E_2 at intervals of 0.005. The best fit location is beneath the new lava dome.

components, has residual errors $E_1 = 0.51$ and $E_2 = 0.84$ (Table 1). The contours around the best fit point in Figure 11 are defined for intervals of 0.005 above the E_2 minimum. While we do not compute formal uncertainties, the error volume defined by a given error level above the minimum can be used to estimate the relative uncertainties in x, y, and z. If the 0.02 ($\sim$2% above the minimum E_2 value) contour is used as an estimate of the uncertainty in the best fit location, the spatial uncertainty estimates for the point-source location are ±80 m in the east-west direction, ±80 m in the north-south direction, and ±100 m in the vertical direction. At a level of 0.05 above the minimum ($\sim$6% above the minimum E_2 value, not shown in Figure 11), the uncertainties are ±140 m in the east-west direction and ±220 m in the vertical direction. The north-south error volume is asymmetric, with a greater extent to the south (280 m) than to the north (100 m). At this error level, the synthetic waveforms begin to look quite different from the best fit synthetics.

[46] The largest misfits occur at stations S01 and S19, where horizontal amplitudes are generally larger than the model predictions (Figure 12). Most stations were placed on fairly competent lava flows, but these two stations were buried in pumice fall from the 1980 eruption. While the depth of unconsolidated pumice beneath these stations is not expected to be large, it may be thick enough to produce site amplification affects that we do not account for with the simplified velocity and density structure we used to compute Green functions.

[47] We also solved for different source mechanisms, including those with six moment-tensor components only and three single forces only. These models produce much larger errors and AIC values than those of the combined moment tensor plus single forces, as shown in Table 1. This demonstrates that the combination of moment tensor and single forces is necessary to explain the data.

[48] The moment tensor found for the best fit model is dominated by the three dipole components (Figure 13a) and a vertical single-force component (Figure 13b). The dipole components are in phase and there is very little energy on the shear components, indicating the mechanism represents a volumetric source. We analyze the moment tensor using point-by-point eigenvalue decomposition. We plotted the eigenvectors, scaled by their corresponding eigenvalues, for each point in Figure 13c, although values less than 30% of the peak value are not plotted for clarity. The eigenvectors

Table 1. LP Inversion Results

Inverted Parameters	E_1	E_2	AIC(E_1)	AIC(E_2)
3 forces	0.820	0.954	−72811	−15941
6 moment	0.672	0.947	−146223	−16649
3 forces + 6 moment	0.511	0.837	**−241784**	**−61245**
30° 270° crack + 3 forces[a]	0.752	0.912	−105008	−32167
5° 340° crack + 3 forces	0.762	0.928	−98261	−25496

[a]The errors are computed using 23 channels of data with equations 8 and 9. Bold numbers indicate the minimum AIC obtained. The eigenvector statistics of this mechanism do not match those of the free inversion.
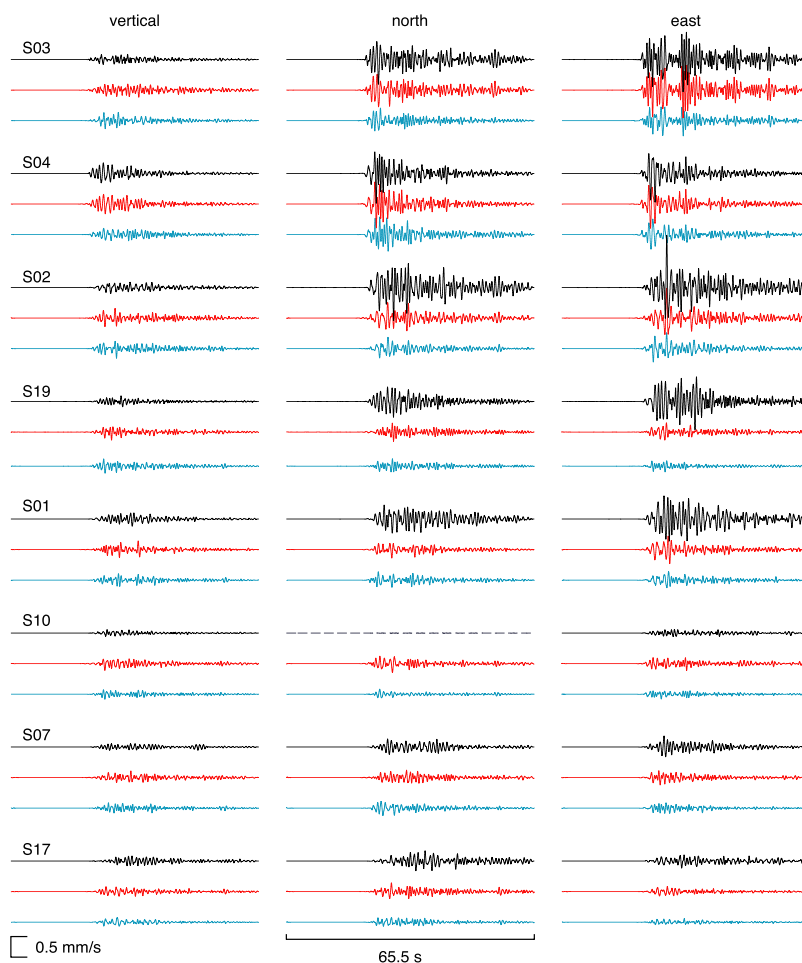
Figure 12. Velocity data from the 2 July 2005 LP event used in the inversion are shown in black; one channel that was not used in the inversion is plotted with a dashed line. Synthetic waveforms for a source with six moment plus three single-force components are in red (see Figure 13). Also, synthetic waveforms for a model of a NNW-dipping crack ($\phi = 340°$, $\theta = 5°$) plus single forces are plotted in cyan (see Figure 15). Both models fit the closest stations (S03 and S04) well, but there is significant degradation in the fits at stations S01 and S19. These stations are buried in a pumice layer of unknown depth and may have strong site amplification. More distant stations are not fit perfectly, but amplitudes are equivalent.

indicate the mechanism is fairly stable with time, although there is some rotation, especially of the intermediate and minimum eigenvectors. The instability could be due to a source complexity, an artifact of source mislocation, or inadequate sampling of the wavefield [see, e.g., *Kumagai et al.*, 2002].

[49] The three components of a diagonalized moment tensor representing a tensile crack have amplitudes $\lambda\Delta V$, $\lambda\Delta V$, and $(\lambda + 2\mu)\Delta V$, where λ and μ are the Lamé constants of the host rock and ΔV represents the volume change associated with the crack opening or closing [*Aki and Richards*, 1980; *Chouet*, 1996b]. If we assume the crack wall rock behaves as a Poisson solid ($\lambda = \mu$), the ratios of the principal axes are [1:1:3], very close to those of our diagonalized moment tensor. A moment tensor of a crack having a higher Poisson ratio of 1/3, $\lambda = 2\mu$, would have ratios of [1:1:2]. The higher Poisson ratio may be appropriate for a hot, magma-filled crack, while a cooler,

steam-filled crack would more likely behave as a Poisson solid.

[50] For the peak value of the maximum eigenvalue, the minimum, intermediate and maximum eigenvalues of the LP source model are [1.01:1.18:3.00] (scaled by 9.22×10^{12} Nm). These ratios are nearly the same as those predicted for a tensile crack in a Poisson solid (Poisson ratio, $\nu = 1/4$). We describe the orientation of the crack by the normal to the crack plane (i.e., the maximum eigenvector) where the azimuth, ϕ, is measured clockwise from north and the plunge, θ, is measured from vertical (Figure 14). The orientation of the vector normal to the crack plane in this model is $\phi = 354°$ and $\theta = 14°$ with the crack dipping 14°, 6° west of north.

[51] We can also estimate the transient maximum volume change during one oscillation in the moment tensor source time function using the crack model. We estimate $\mu = 12$ GPa using an average shear wave velocity of 2.44 km/s and density of 2070 kg/m³ from samples of Mt. Unzen dacite
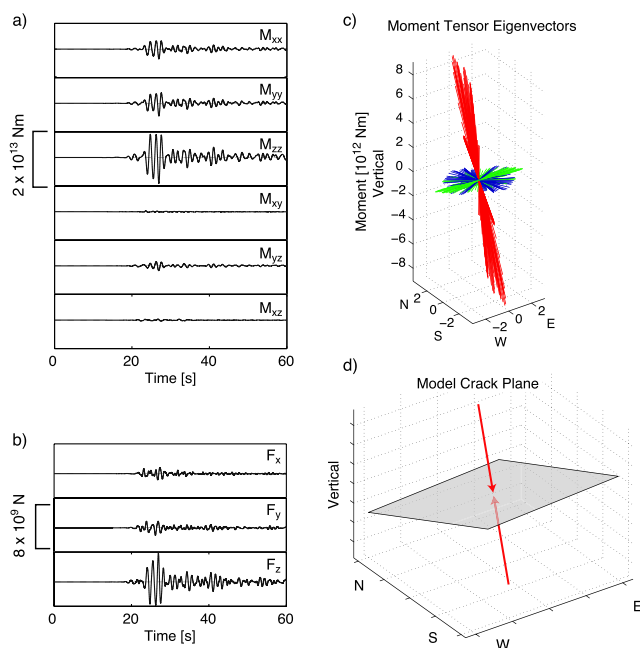
Figure 13. The source time function of the 2 July LP event is dominated by the dipole components of the moment tensor (a) and a vertical single force (b). The moment tensor dipole components are in phase, indicative of a volumetric source. Point-by-point eigenvector analysis of the moment tensor source time function shows a consistent relationship between the three eigenvectors with a ratio near 3:1:1. The maximum (red), intermediate (blue) and minimum (green) eigenvectors, scaled by the eigenvalues, are plotted in Figure 13c and a model that satisfies the moment tensor, a tension crack in a Poisson solid, is plotted normal to the maximum eigenvector in Figure 13d.

having porosities of $4-26\%$, measured at low temperature and low pressure [*Scheu et al.*, 2006]. Assuming $\lambda = \mu$, we find $\Delta V = 770$ m^3. For a crack with dimensions 100 m × 200 m, this could represent opening or closing of ~4 cm.

[52] The vertical-force component, which peaks at 8 GN, may be explained by oscillations of the growing spine and possibly the entire dome. These oscillations represent disruptions in the otherwise smooth extrusion of the dome. If we assume the force is evenly distributed over a conduit with a minimum 50 m radius (*Iverson et al.* [2006] use 100 m), we obtain an average pressure of ~1 MPa. In early July 2005 the dome was 2365 m high [*Schilling et al.*, 2008], so the maximum dome elevation was more than 350 m above the imaged crack. On the basis of this maximum dome height, we find the lithostatic pressure on the subjacent crack is on the order of 8 MPa, assuming dome rock with a density of 2300 kg/m^3 [e.g., *Pallister et al.*, 2008]. This is nearly an order of magnitude larger than the maximum amplitude of the pressure fluctuation estimated above.

[53] We test the model of a subhorizontal crack by inverting the Green functions for cracks of many orientations plus three single forces. The crack moment tensors are calculated using equation (15) of *Chouet* [1996b] and assuming $\lambda = \mu$. Using a grid search, we obtain a source time function for each crack and set of forces for cracks with the following orientations: we use 5° increments for θ

over the interval $0° \leq \theta \leq 45°$ and we use 10° increments for ϕ over the intervals $180° \leq \phi \leq 360°$ plus $0° \leq \phi \leq 30°$. The source time functions for each mechanism are multiplied by the theoretical moment tensor to obtain the source time functions for the tensor components. The source time functions from these tensor components and the single forces are then compared with those obtained in the original inversion with nine free parameters.

[54] We found a best fitting crack oriented with a dip of 30° to the west ($\phi = 270°$, $\theta = 30°$, see Table 1). While this is our best model in terms of the waveform fit, it does not agree with the crack orientation predicted by the free inversion. An east-west oscillating force dominates the single-force components and there is relatively little north-south or vertical force. In order to find a crack and set of single forces that match our free inversion solution, we conducted a grid search for source time function reconstructions that give eigenvectors similar to those of the free inversion. The eigenvectors were computed for each point in the source time functions and the results were binned in 5° bins for comparison with those from the free inversion. A model was considered to match the eigenvector statistics of the free inversion when the corresponding values of θ and ϕ are within 5° of those of the free inversion.

[55] The best model crack having statistics that match those of the free inversion is gently dipping to the NNW ($\theta = 5°$, $\phi = 340°$). The source time function for this model is plotted in Figure 15. The maximum volume change estimated for this crack is about 600 m^3, somewhat less than the volume change predicted by the maximum eigenvalues of the full moment-tensor inversion. The synthetic waveforms from this model are plotted in cyan in Figure 12. The waveform fits are not as good as those for the free inversion; even though there are fewer parameters, the AIC value is much larger than the AIC for the free inversion (see Table 1). Note that even our best fitting single crack has an AIC value that is larger than the AIC of the free inversion. However, the AIC for a crack plus three forces, obtained using error E_2, is better than either the moment-only or the single-forces-only inversions.

[56] One reason our single crack model does not fit the data as well as the full moment tensor may be due to unmodeled source complexity. While the eigenvectors plotted in Figure 13c clearly indicate a source dominated by a
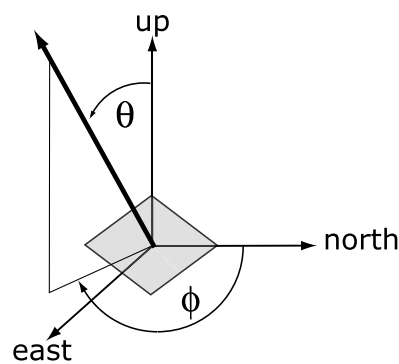

Figure 14. Coordinate system used to describe the crack orientations. Cracks are described based on the pole to the plane, where the azimuth, ϕ, is measured clockwise from north and the plunge, θ, is measured from vertical.
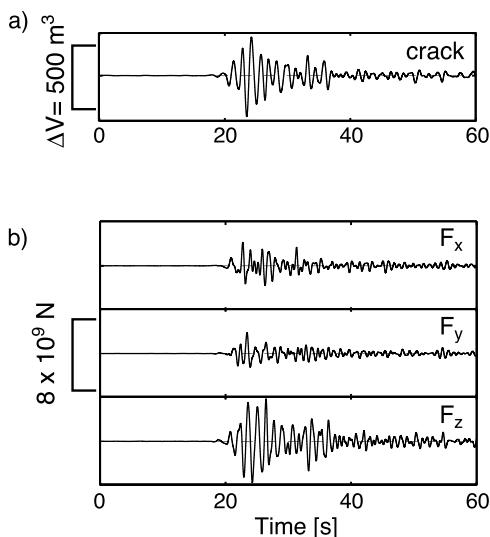
a)

b)

Figure 15. The source time function of the 2 July LP assuming a NNW-dipping crack (a) plus single forces (b). The volume change in the crack is calculated assuming $\mu = 12$ GPa.

subhorizontal crack, there is scatter in the eigenvectors suggesting the involvement of subdominant sources. In addition, the ratio of the eigenvalues is not exactly [1:1:3] as predicted for a tension crack in a Poisson solid, but [1.01:1.18:3.00]. Thus the source is likely composed of a composite of one or more volumetric sources in addition to the dominant subhorizontal crack. For example, a dendritic steam exhaust pathway leading to the surface could contribute seismic energy that we cannot model with a single crack. Other coincident seismic sources could involve cracking and/or crumbling of the dome. Photographs taken from a remote camera near station S01 [*Poland et al.*, 2008] show that a large piece fell from the top of the dome at around the time of the modeled earthquake.

[57] In addition to neglecting possible sources, our modeling is limited by the point-source approximation. The crack is spatially separated from the dome, the movement of which we infer as the primary source of the single forces. To investigate the sensitivity of this on the waveforms and source time functions, we performed additional grid searches for two separate point sources that were moved independently: 1) the six independent moment-tensor components comprised one point source and 2) the three single-force components comprised the other. The search was performed over a 200 m × 200 m × 200 m region surrounding the best fit point-source location. The results showed only minor changes to the source time functions and no notable improvements in waveform fit. We concluded that this spatial separation is insignificant and that the additional complexity of two point sources was unjustified. We note that progress has been made in the inversion of LP waveforms for cracks with finite dimensions [*Nakano et al.*, 2007], but we reserve such an investigation of the Mount St. Helens data for a future study.

3.4.2. VLP Band

[58] We modeled the VLP band (8–40 s) of the same 2 July 2005 event, because it produced clear signals at the nearest stations and was recorded by all stations except S20, which was inoperative at the time. Our grid search for the best fit source location using six moment plus three single-force components yields a position just southwest of the 1980s dome at 1750 m elevation (Figure 16). This position is about 350 m below the top of the 1980s dome. The minimum residual errors for this best fit location, determined with 24 channels, are $E_1 = 0.092$ and $E_2 = 0.343$ (see Table 2). The contours in Figure 16 are at 0.005 intervals above the E_2 minimum. The error volume defined by the 0.02 contour gives an uncertainty estimate of (120 m in the east-west direction, (100 m in the north-south direction, and (140 m in the vertical direction.

[59] The data and synthetic waveforms for the inversion at the best fit point-source location are shown in black and red, respectively, in Figure 17. Channels that were deemed too noisy are not shown, or are shown with dashed lines and were not used in the inversion. The VLP signal was indiscernible on the horizontal channels of the most distant stations, S12, S13, S14, S15, and S16. The north channel of station S10 was not functioning properly. The large horizontal velocities at stations S02, S03, and S04 are the most important in terms of fitting a mechanism, but we fit most of the channels on stations up to 4 km away quite well with this mechanism. Minor differences are found on the vertical components of stations S02 and S04 and on the horizontal components of several stations. Neither the noisy north-south channel nor the east-west channel of station S19 is fitted well. We find that the general characteristics of the moment tensor, described below, are similar whether just the three stations with the highest signal-to-noise ratio are used in the inversion, or all but the noisiest channels shown in Figure 17 are inverted.

[60] The source time functions of the moment-tensor components and single forces for the best fit model are shown in Figure 18. The volumetric components of the moment tensor dominate with only minor contributions from the off-diagonal components, which are slightly out of phase compared to the dipole components. The three volumetric components are in phase and the amplitude of the vertical dipole component, M_{zz}, is more than twice that of the east, M_{xx}, or north, M_{yy}, components. In addition, there is a significant single-force component in the east direction.

[61] The ratio of the peak-to-peak amplitudes M_{xx}/F_x is 9090 m. We found that the relative contributions of the moment-tensor and single-force components vary by station and source position. For example, the relative amplitudes of the east-west components of the Green functions due to an eastward force (F_x) of 1 N and east-west dipole (M_{xx}) of 1 Nm at the same location, ranges by station from 285 to 2035 m. Because there is not a clear dependence on epicentral distance, we attribute this variation as primarily due to the effects of topography. For the best fit location, this implies that the contribution of F_x relative to M_{xx} is between 3% and 22% of the east-west component synthetic waveform amplitudes. By comparison, F_z contributes about 2% to the synthetic vertical waveforms relative to M_{zz}. This suggests that the single-force component contributions are generally minor compared with the moment components. Despite this, we find that the combination of moment tensor and single forces are necessary for explaining the data based
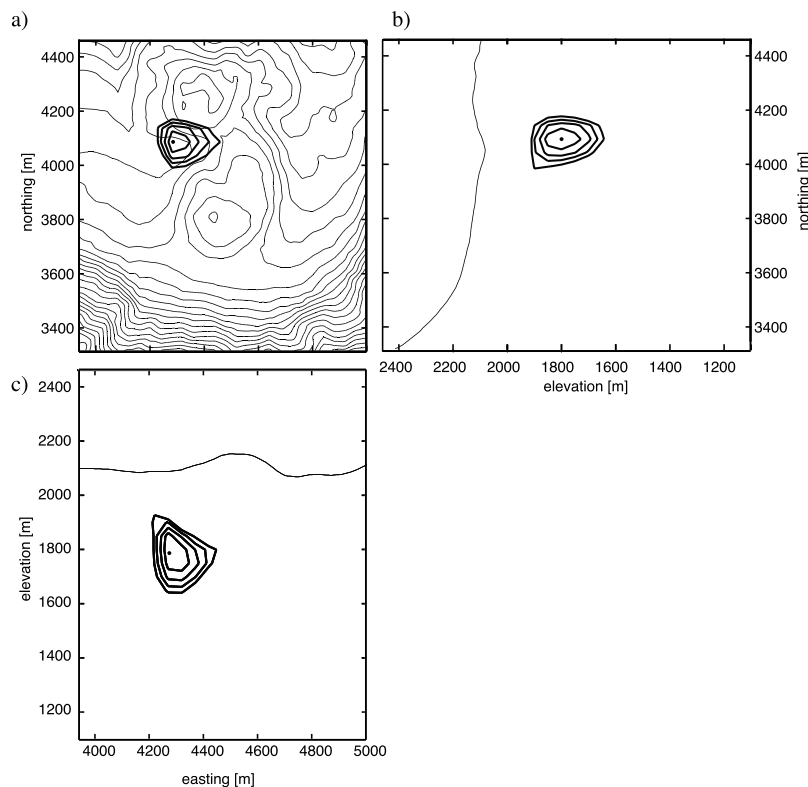
a)

b)

c)

Figure 16. Location of the point source (solid dot) yielding the minimum residual error for the 2 July 2005 VLP event. Thin lines in (a) show topographic contours (20 m spacing) within the crater as of April 2005. Heavy lines in all three parts contour E_2 at intervals of 0.005. The best fit location is beneath the southwestern end of the 1980s lava dome.

on the AIC (Table 2). A significant contribution from the single-force components, particularly F_x, is necessary for a good waveform fit on a subset of stations.

[62] As with the LP source, we can obtain an estimate of the eigenvectors for the moment-tensor components from the maximum peak-to-trough amplitudes of the source time functions. The principal axes of the moment tensor have axes (eigenvalues) [0.77:0.79:2.00] (scaled by 1.47 × 10^{13} Nm) and the dominant dipole is ∼10° from vertical. We may obtain ratios of the principal axes of the moment tensor of [0.78:0.78:2.00] for a crack with a Poisson ratio, ν = 0.28. This is very close to the corresponding values in our solution of [0.77:0.79:2.00] and suggests our moment tensor may represent a single sill. The eigenvector for the dominant component indicates this sill is dipping 12°, 7° west of north ($\theta = 12°$ and $\phi = 353°$ in the coordinate system shown in Figure 14). We discuss a test of this model below.

[63] Estimating the eigenvectors from just the peak amplitudes of the moment tensor assumes that the source time functions of individual moment components all have the same shape. The off-diagonal components are clearly different from the diagonal components (Figure 18), and thus this simplified approach may overlook important information in the source time function. A more detailed approach is to consider the time-dependent properties of the eigenvectors by computing eigenvectors and eigenvalues at each point in the source time function. Values less than 30% of the peak value are not used. The point-by-point analysis yields a mean dominant eigenvector that is slightly different

from the dominant eigenvector found above. Figures 19a and 19b show rose diagrams for the dominant, intermediate, and minimum eigenvectors sorted into 5° bins.

[64] Histograms of the ratios of the smallest to dominant and intermediate to dominant eigenvalues are shown in Figures 19c and 19d, respectively. The weighted arithmetic mean, $\bar{x}$, of these ratios (with one standard deviation given in parentheses) [0.62(0.06):0.88(0.07):2.00] are different from the ratios found with the maximum peak to trough measurement. If we normalize to 3, the ratios are [0.93(0.10):1.32(0.10):3.00]. At one standard deviation, the mean minimum and intermediate eigenvalues are significantly different. We can derive a mechanism with these eigenvalue ratios if we consider the volume changes in two

Table 2. VLP Inversion Results

Inverted Parameters	E_1	E_2	AIC(E_1)	AIC(E_2)
3 forces	0.337	1.123	−204491	22083
6 moment	0.194	0.616	−308521	−90945
3 forces + 6 moment	0.092	0.343	**−448569**	**−201034**
Crack + 3 forces	0.247	0.884	−263219	−22975
Crack + pipe + 3 forces[a]	0.124	0.493	−392993	−132936
2 cracks + 3 forces[a]	0.125	0.498	−391480	−131035
Crack + pipe + 3 forces	0.155	0.501	−350707	−130031
Sill + dike + 3 forces	0.140	0.500	−370531	−130469

[a]The errors are computed using 24 data channels with equations 8 and 9. Bold numbers indicate the minimum AIC obtained. The eigenvector statistics of these mechanisms do not match those of the free inversion.
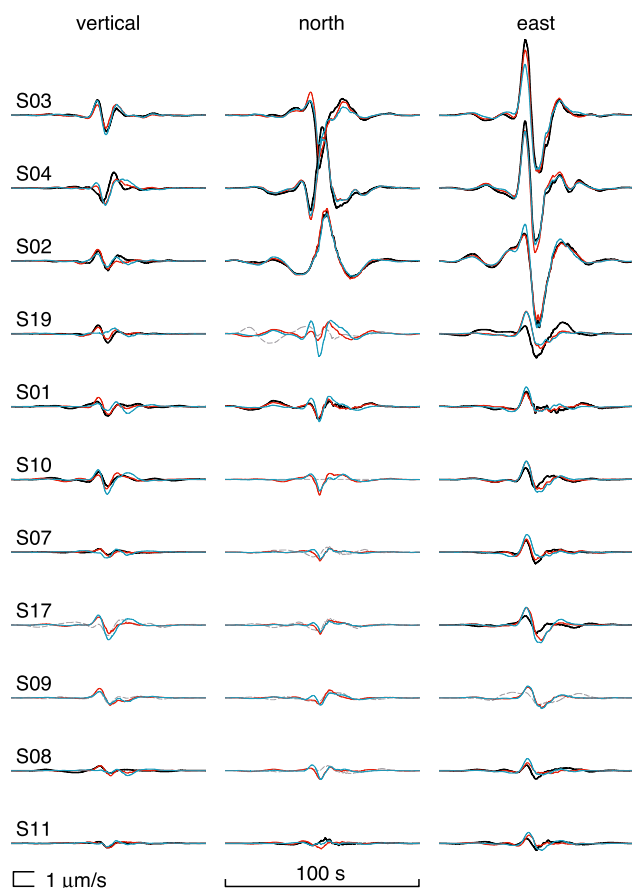
Figure 17. Velocity data from the 2 July 2005 VLP event used in the inversion are shown in black; channels that were not used in the inversion due to low signal-to-noise, are plotted with dashed lines. Synthetic waveforms for a source with six moment plus three single-force components are in red (see Figure 18). Synthetic waveforms for a sill-dike model ($\theta_1 = 25°$, $\phi_1 = 335°$, $\theta_2 = 70°$, and $\phi_2 = 165°$) plus single forces (Figure 19) are plotted in cyan. Both models fit the closest stations (S01, S02, S03 and S04) well, but S19 does not fit well.

Figure 18. The source time function of the 2 July VLP event is dominated by the dipole components of the moment tensor, particularly, M_{zz} (a), and a large eastward single force (b). The moment tensor dipole components are in phase, indicative of a volumetric source.

cracks with different orientations, which combine to make up one source time function. In addition to different orientations, the amplitudes and signs of the deformation in the two cracks may differ. For example, if we assume a Poisson ratio $\nu = 1/3$, a value appropriate for andesite near liquidus temperatures [*Murase and McBirney*, 1973] that may apply to a dacite magma-filled crack, we obtain ratios with the matrix operation $[1{:}1{:}2] - 0.2 \times [2{:}1{:}1] = [0.6{:}0.8{:}1.8]$. After normalization, the ratios become $[0.67{:}0.89{:}2.00]$, a result close to the mean values from the point-by-point analysis. This combination suggests a composite source including a shallow-dipping sill and a near-vertical, approximately east-west-striking dike. Because we are subtracting one tensor from another, the volume changes in the two cracks have the opposite sign. That is, when the sill is inflating, the dike is deflating.

[65] Similarly, we can arrive at ratios close to those predicted from the free inversion through combination of a sill and a quasivertical, radially expanding pipe. The axis
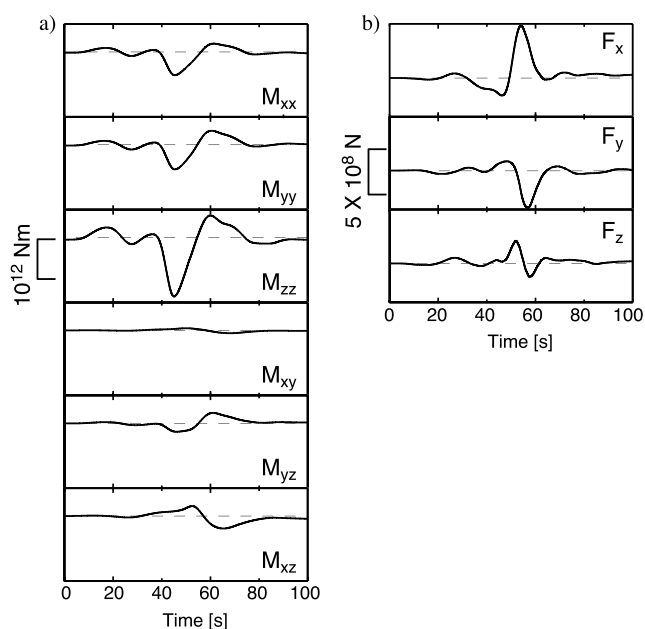

Figure 19. Histograms of the point-by-point eigenvector analysis of the VLP moment tensor source time function (a and b). The maximum (M), intermediate (I), and minimum (m) eigenvectors are plotted with black, gray, and white, respectively. Histograms show the relative size of the minimum (c) and intermediate (d) eigenvalues with respect to a maximum eigenvalue normalized to 2. The mean values are printed in each box. These plots highlight the consistency of the moment tensor.

of such a pipe is described by the same θ and ϕ used to orient the normal to the tension crack. For $\nu = 1/3$, the ratios of the principal axes of a pipe are [1.5:1.5:1.0] where the smaller value is parallel to the axis [*Chouet*, 1996b]. We can construct the following combined source: [1:1:2] − 0.2 × [1.5:1.5:1.0], which yields [0.78:0.78:2.00] after normalizing. Note that this result is the same as that obtained for a single tension crack with $\nu = 0.28$, demonstrating the nonuniqueness of the solutions. As with the sill and dike composite source, the secondary source in this case (pipe) has the opposite sign of volume change as the dominant sill.

[66] We test the single-crack, two-crack, and crack-pipe source models by inverting for Green functions for these volumetric sources plus three single forces. The crack and pipe moment tensors are calculated using equations (15) and (16) of *Chouet* [1996b], respectively, with $\lambda = 2\mu(\nu = 1/3)$. We obtain a source time function for each moment and force. The source time functions for each moment are multiplied by the theoretical moment tensor to reconstruct the source time functions for the moment-tensor components. In the case of two cracks, or one crack and one pipe, the individual tensor source time functions are summed to obtain the combined point-source tensor. The source time functions from these tensor components and the single forces are then compared with those obtained in the original inversion with nine free parameters.

[67] While the eigenvector statistics give an indication of the orientation of our theoretical crack(s), we conduct a grid search over many combinations of crack/pipe orientations to look for other models that may fit equally as well or better. We calculate Green functions for crack mechanisms of all possible orientations, incremented by 10° for θ and 15° for ϕ initially. For a single crack, we have 240 orientations to examine. For a sill ($\theta \leq 40°$) plus a dike ($\theta \geq 50°$), we have 14,400 combinations. The grid spacing is then reduced to 5° for both θ and ϕ around crack orientations that yield minimum residual values.

[68] The best fitting single crack has orientation $\theta = 30°$ and $\phi = 0°$ and yields residual errors $E_1 = 0.247$ and $E_2 = 0.884$ (Table 2). These error values are much higher than the minimum errors obtained from the inversion with nine free parameters. The AIC values also indicate that a model having a larger number of parameters is necessary (Table 2). While a single crack represents a plausible physical model, a combination of two cracks may be required to fit the data.

[69] The best fitting model that combines a crack and a pipe produces low residual errors, $E_1 = 0.124$ and $E_2 = 0.493$ (Table 2). This model consists of a northwest-dipping crack ($\theta_1 = 40°$, $\phi_1 = 320°$) and a nearly flat-lying pipe plunging to the northeast ($\theta_2 = 80°$, and $\phi_2 = 220°$). The AIC values for this solution are higher than those obtained with the nine free-parameter inversion, but are lower than the AIC values for a single crack plus forces, moment-only solutions, and single-force-only solutions. However, the reconstructed moment tensor source time functions and the eigenvector statistics derived from them are significantly different from those of the free inversion.

[70] We find a similar situation for the best fitting two-crack model. The residual errors are nearly the same as the best crack plus pipe model at $E_1 = 0.125$ and $E_2 = 0.498$ for steeply dipping cracks 1 ($\theta_1 = 40°$, $\phi_1 = 315°$) and 2 ($\theta_2 = 50°$, and $\phi_2 = 135°$) and the AIC values are likewise similar.

But again, the reconstructed moment tensor source time functions and the eigenvector statistics derived from them are significantly different from those of the free inversion. If we require our crack model to also have the same statistics as the free inversion, as we did with the LP crack model, we need a much different set of cracks and source time functions.

[71] We conduct a grid search for source time function reconstructions that produce eigenvectors similar to those of the free inversion as we did with the grid search for minimum residual above. The moment-tensor source time function is constructed from the sum of the moment tensors of the two cracks (or crack and pipe). Then the point-by-point eigenvector and eigenvalue ratio statistics are binned by 5° as before. A model is considered to match the eigenvector statistics of the free inversion when the corresponding values of θ_1, ϕ_1, θ_2, and ϕ_2 are within 5° of those of the free inversion. In other words, for each of the four angles describing the crack orientations, the bin with the maximum number of points must be within one bin on either side of the best orientation from the free inversion.

[72] Of the crack-pipe models with combined moment-tensor source time functions that match the statistics of the free inversion, the solution with the best fitting model has $E_1 = 0.155$ and $E_2 = 0.501$ (Table 2). The crack is oriented $\theta_1 = 25°$ and $\phi_1 = 330°$ and the pipe is oriented $\theta_2 = 30°$ and $\phi_2 = 240°$ and the eigenvalue ratios of this model are [0.79:0.79:2.00]. Recall that θ_2 and ϕ_2 define the orientation of the pipe axis. We obtain a solution that matches the statistics of the free inversion with only a slight increase in the error and AIC values over the crack-pipe model that yields the smallest errors.

[73] The two-crack model with the lowest residual that also matches the statistics of the free inversion has $E_1 = 0.140$ and $E_2 = 0.500$ (Table 2) when $\theta_1 = 25°$, $\phi_1 = 335°$, $\theta_2 = 70°$, and $\phi_2 = 165°$. The eigenvalue ratios of this model are [0.63:0.88:2.00]. Both the crack-pipe model and two-crack model have similar residual errors and produce waveforms that are indistinguishable, but the ratios of the eigenvalues of the two-crack model are closer to those of the free inversion, [0.62:0.88:2.00]. The synthetic waveforms from the two-crack model are plotted in cyan in Figure 17. Noticeable differences in the fits relative to the free inversion can be seen at station S19 and S01, although most channels have similar synthetics for both the free inversion and inversion with the fixed cracks. Figure 20 shows the source time functions of the two cracks and three single forces. The maximum volume change in the sill, assuming $\mu = 7$ GPa, is ~1000 m^3.

[74] We note that both the two-crack and crack-pipe models yield higher AIC values than does the free inversion. Still, we consider either to be reasonable models for the VLP source. The addition of more stations within 1 km of the source would likely improve the source-centroid estimate and free-inversion source time functions and lead to an improved model of the source.

3.4.3. Other LP and VLP Events

[75] In addition to the well-studied event on 2 July 2005, we modeled LP and VLP earthquakes from other days and times for a total of 68 LP events and 5 VLP events. Our waveform cross-correlation analysis reveals similarity among most of the LP events, but shows subtle differences
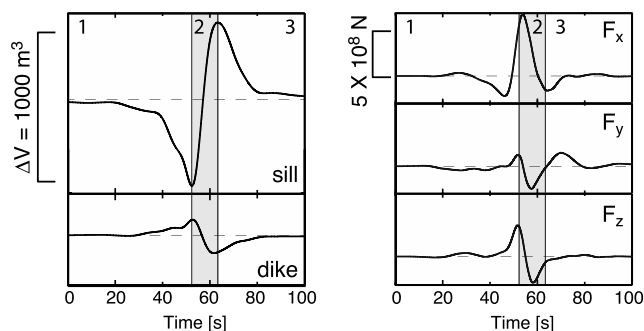
Figure 20. The source time function of the 2 July VLP assuming a sill-dike model ($\theta_1 = 25°$, $\phi_1 = 335°$, $\theta_2 = 70°$, and $\phi_2 = 165°$) plus single forces. The numbers refer to the three stages of sill deformation: initial deflation (1), inflation (2), and deflation (3). The maximum sill volume change of 1000 m^3 is calculated assuming $\mu = 7$ GPa.

over time. We chose to model events from 3 days to examine whether the source time function varies with time. Events from 2, 12 and 22 July, which correlate with the 16 June reference event at a cross-correlation coefficient of 0.95 or higher, were modeled. This included small (M < 2), typical drumbeat events. During this time period, stations S01, S02, S03, and S04 were all operating normally. Problems with stations S01 and S03 later in the summer and fall prevent comparisons of waveform inversions for those time periods.

[76] While many of the smaller events have a low signal-to-noise ratio at the more distant stations, the best fit locations and source time functions are nearly identical to those of the 2 July event, indicating the repeated activation of the same source. In each of these mechanisms, the moment tensor is dominated by a volumetric component that is consistent with a northerly dipping crack, and F_z dominates the single-force components. We also inverted for stacks of similar LP events and found the same mechanism. Minimum uncertainties for most of the LP events and stacks of events modeled are $0.4-0.5$ for E_1 and $0.8-0.9$ for E_2.

[77] Interestingly, we found a subtle shift in the source centroid of the LP events with time. Events from 22 July are located $60-120$ m west of the events recorded earlier in July. This shift coincides with the transition to growth of a new spine west of the spines active during, and prior to, early July 2005 [see, e.g., *Moran et al.*, 2008; *Vallance et al.*, 2008]. The areal extent of the resonating crack may not have changed, but the center of mass of the overlying dome shifted to the west, resulting in a change in the source centroid. The triggering mechanism may have also changed as a result of the new dome position.

[78] Most of the remaining VLP events we inverted for did not produce a clear mechanism. This is attributed to the weak signals and low signal-to-noise ratio in the records. The four additional events we were able to model produced minimum-residual solutions for point source locations within 120 m of the 2 July 2005 event. These occurred on 5, 22, 23, and 25 July 2005. The four key stations (S01, S02, S03 and S04) were not operating simultaneously after 26 July. In addition to locations consistent with the 2 July event, each

of these four VLP events produced a mechanism compatible with a dominant sill plus subsidiary dike or pipe mechanism. The key differences were in the single-force components, which were much smaller in magnitude and/or noisier than the force components of the 2 July event. In some cases, the F_y component was the largest single force.

[79] We estimate an average volume change based on the amplitude ratio of the VLP signals recorded for the large 2 July event and more typical events recorded during July 2005. In general, the amplitude of the smaller events observed at S03 is a factor of 5 smaller than the large event. If we assume the same sill-dike mechanism, this implies a volume change of 200 m^3 in the sill for smaller events. Given the average rate of 1 event every 5 min, we get an average volume change rate of 0.7 m^3/s, which is similar to the extrusion rate measured at the surface using air photos [*Schilling et al.*, 2008]. However, our estimate from the VLP data should not be interpreted as an average flow rate because most of the volume change in the model sill is perpendicular to the flow direction.

4. Source Process

[80] The LP and VLP sources seem to be linked, at least during some time periods (Figure 7), but best fit locations of these events are distinct. The LP source is very shallow, at about 2000 m elevation and directly beneath the growing dome. The VLP source is 250 m deeper and 400 m NNW, beneath the SW end of the old 1980s lava dome. Interestingly, the line joining those two points dips at about 30° to the NNW, similar to the orientations of both the LP-source crack and the dominant VLP-source sill.

[81] The LP source does not seem to be within the eruption conduit, as the vent is near the southern edge of the 1980s dome [e.g., *Vallance et al.*, 2008]. The modeled crack could be along a preexisting zone of weakness that separates two older lava flows, for example. The most likely fluid in the crack is steam, owing to the abundant water, in the glacier and exsolved from the magma, and heat from the magma. Airborne surveys have detected relatively low levels of magmatic gases [*Gerlach et al.*, 2008]. Also, while no discrete pulses of steam have been observed (S. Moran, personal communication, 2007) photos of the growing lava dome show steam effusing from multiple points near the base of the dome and from within the dome.

[82] The ratios of the eigenvalues for the LP moment tensor are consistent with a steam-filled crack. We would expect that a hotter, magma-filled crack would have a higher Poisson ratio and therefore the ratio of maximum to intermediate and minimum eigenvalues would be smaller. In addition, analysis of the complex frequencies of selected LP events is consistent with a steam-filled crack. We applied the Sompi method [*Kumazawa et al.*, 1990] to the source time function of our model crack and found growth rates for our dominant frequency that are consistent with low Q values of $10-20$. Such high attenuation can be attributed to bubbly magma, bubbly water, or steam [e.g., *Kumagai and Chouet*, 2000; *Kumagai et al.*, 2005]. Given the position of our crack, it is unlikely to be filled with bubbly magma. Instead, steam or a mixture of bubbly water and steam are more likely to be filling the crack.
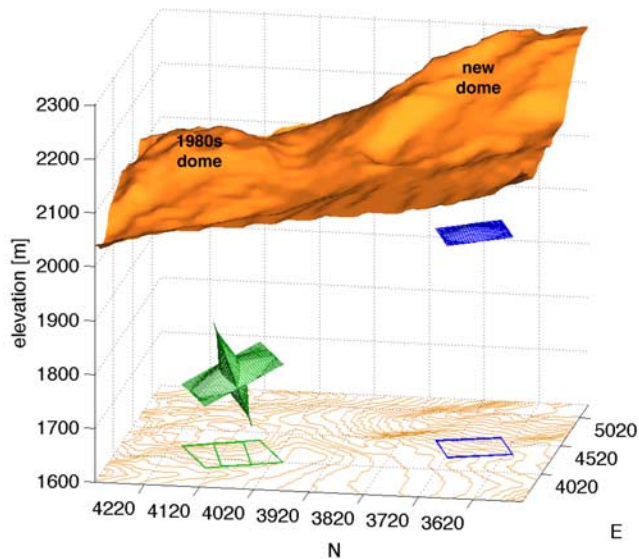
Figure 21. East-northeast, three-dimensional, perspective view of the LP crack (blue) and VLP sill-dike (green) sources. Topography is shown as a surface and is contoured on the bottom at 20 m. Distances are in m and are relative to the origin of the 20-m-grid model used to calculate Green functions.

[83] A possible scenario for the LP events we model involves the repeated pressurization of a subhorizontal crack that lies beneath the southern crater and new lava dome. Steam generated by heating groundwater, in addition to exsolved steam from the magma, are fed into the crack, gradually expanding and pressurizing it. The southern, updip end of the crack must be sealed to prevent steam from escaping. When a pressure threshold is reached, some steam is forced out of the crack through fractures that eventually lead to the surface or out to the glacier-crater floor interface. The loss of pressure triggers a partial collapse of the crack, which then resonates for 5 seconds to 10s of seconds. The collapse of the crack produces the dilatational first motions recorded on all of the broadband stations.

[84] We note that *Matoza et al.* [2007] observed infrasound expressions of the LP events intermittently in November 2004. These recordings, which were made at a station 13 km north of Mount St. Helens, mimic the waveform and temporal sequence of the seismic equivalents. The infrasound component of the signal indicates that the LP source is very shallow, consistent with our source modeling. *Matoza et al.* [2007] present three possible models for generation of the infrasound signal: oscillations of a piston at the ground-air interface; oscillations in the LP source fluid-crack system that produce a pressure wave in the air; or a rapid release of gas which travels though permeable medium to the surface to generate the infrasound waves. Each of these models is compatible with the LP source model of a steam-filled crack and/or oscillations of the spine.

[85] The VLP source can be represented as a combination of a sill and dike or pipe. For simplicity in the discussion, we will assume the dike or pipe is a fat crack, which we will call a dike. While we assume a point source, the dike is more likely above or below the sill. Given the dike orientation predicted by our modeling, it does not seem reasonable to have the sill below the dike, as the dike is dipping steeply to the SSE. This would produce a very sharp corner and would be inconsistent with the relative locations of the VLP source and vent. The dike is more likely below the sill and could represent the top of the old conduit that fed the 1980s dome-building eruptions. During the start of the eruption in September 2004, material moving up through (or adjacent to) the conduit found an easier pathway to the surface by breaking out of the conduit near the surface and pushing out to the south, rather than intruding the 1980s dome. The modeled sill represents this new portion of the conduit.

[86] The relationship between the shallow hydrothermal crack that is the source of the LP earthquake resonance and the deeper sill-dike system is not straightforward to interpret. In Figure 21 we offer a perspective view of the two sources. Note that the same velocity model was used to locate both point sources. We propose that the collapse of the LP crack and related sagging of the dome triggers a response in the magma conduit that we see in the VLP band. We interpret the single-force components of the VLP as due to mass advection within the magma conduit. Mass acceleration in one direction will produce a reaction force in the Earth in the opposite direction, while mass deceleration in one direction will produce a reaction force in the Earth in the same direction [see, e.g., *Takei and Kumazawa*, 1994].

[87] We note here that linear momentum must be conserved during this event, but we cannot necessarily see all of the forces involved. For example, upward acceleration of the center of mass of the source volume may be opposed by weak, upward, frictional forces applied over a large extent of the conduit at depth. Conversely, decreased downward frictional forces may oppose upward deceleration. These frictional forces may be difficult to image if they are applied over a portion of conduit much larger than the two cracks we model. The magma is also somewhat compliant, so that some of the opposing forces are involved with compression of the magma deeper in the conduit.

[88] Our interpretation of the single-force components is complicated by the fact that we have two cracks within which the forces can operate. In general, we interpret the horizontal forces as acting in the subhorizontal sill and the vertical force as acting in the dike. We assume a constant background flow velocity upward through the dike and southeastward sill so that the forces represent changes in the steady state velocity. This leads to a coherent relationship between changes in flow rate and crack volume changes.

[89] During the first phase of the VLP event, the sill deflated and the dike inflated (part 1 in Figure 20). The single-force components are fairly unstable during this first phase; the amplitude of the F_y component, in particular, is dependent on the dike orientation and varies depending on whether the dike is striking west or WSW. If we assume a constant background velocity of material up through the dike and into the sill, the upward vertical force could represent upward deceleration of the magma in response to the deflating sill. So we are seeing a decrease in the velocity of the magma through the conduit below the sill.

Correspondingly, the horizontal forces represent deviations from this SSE-directed motion consistent with material moving out of the sill faster than the background rate. The westward force and subsequent eastward force during this phase are interpreted as an increase in the eastward velocity, followed by eastward deceleration. Similarly, the small northward force during this phase represents acceleration to the south.

[90] During sill inflation-dike deflation (part 2 in Figure 20), the single forces are stable for various dike orientations. The horizontal components indicate a decreasing eastward force and decreasing northward followed by increasing southward force. These forces are consistent with slowing of magma as the sill inflates. The vertical force changes from upward to downward during the first half of the sill inflation, possibly indicating a change from upward deceleration to upward acceleration of mass through the dike. All three single-force components are relatively small during the last sill deflation-dike inflation phase of the VLP event (part 3 in Figure 20), but the horizontal forces are consistent with acceleration of magma through the conduit and a return to the background flow rate.

[91] We estimate the strain rate associated with the implied deformation of the conduit in order to evaluate if the model is physically reasonable. The total transient volume change for the sill is estimated to be on the order of 1000 m^3. If we assume the sill is 150 by 150 m, this volume change represents a total opening of <5 cm. If the sill is 10 m thick, a fairly low estimate, this is only 0.5% change in the thickness of the sill. We can use these values to estimate a strain rate and an upper bound on the viscosity of the material. Since the sill inflation takes about 15 seconds, the strain rate is on the order 10^{-4} s^{-1}. If we assume the shear viscosity (η), shear strain rate ($\dot{\varepsilon}$), shear strength relationship for brittle failure of melt in the glass transition of [*Tuffen and Dingwell*, 2005], $\eta\dot{\varepsilon} < 10^8$ Pa, we find a viscosity upper bound of 10^{12} Pa s. This is within the range of reasonable values for dacite magma. Local strain rates are likely to be perhaps an order of magnitude higher than 10^{-4} s^{-1}, which could induce fracturing of magma with viscosities greater than 10^{11} Pa s. Conversely, lower viscosities in the center of the conduit, due to higher temperatures, could accommodate the higher strain rates without brittle failure.

[92] The high viscosity of the erupted lava permits tall spines to grow from the vent when they are supported by older dome material. However, the earliest dome features were whaleback-shaped extrusions that apparently could not support tall spines. We note that the orientations of these early whalebacks are subparallel to the orientation of the imaged VLP sill. Subsequent extrusions piled on top of the earlier material forcing the spines to grow steeper [*Vallance et al.*, 2008]. As we saw in July 2005, a new spine emerged to the west, presumably because the mass of the older spines became too large to move.

[93] Petrologic studies of the Mount St. Helens dome rocks have revealed important structural and rheological details relevant to our interpretation. The exterior of the extruded spines are composed of fault gouge 1–2 m thick [e.g., *Cashman et al.*, 2008; *Pallister et al.*, 2008]. This has been attributed to seismogenic stick slip of the dome and conduit [*Iverson et al.*, 2006], although gouge could form during aseismic slip. The corner in the conduit implied by

the VLP source could promote gouge formation. Occasionally, curvilinear bands of discolored gouge that parallel the contact between the spine and debris apron at the base of the spine have been observed [e.g., *Cashman et al.*, 2008; *Pallister et al.*, 2008]. These "bathtub rings" may represent accumulations formed during transient sagging of the dome related to the collapse of the crack.

[94] Mineralogical indicators in the dome rocks, such as the presence of tridymite in most samples, indicate groundmass crystallization at low pressures (10–25 MPa) and high temperatures (900°C) [*Cashman et al.*, 2008; *Pallister et al.*, 2008]. *Cashman et al.* [2008] and *Pallister et al.* [2008] argue that relatively little crystallization occurs until the magma is <1 km from the surface, where it is driven by extensive degassing rather than cooling. Some of the water degassing at shallow depths may flow up into the resonating LP crack.

[95] The depth of the VLP source, 350 m below the 1980s dome, is consistent with the shallow crystallization implied by the petrology of the erupted lava. If the deformation of the sill and dike indicated by the VLP signal occurs plastically, as we expect, the viscosity of the magma must be low enough to permit strain rates of 10^{-4} s^{-1} without brittle failure. *Zhang et al.* [2003] show that silicic magma viscosity is highly dependent on water concentration, and we infer that the viscosity of Mount St. Helens magma must increase rapidly at shallow depth as it degasses. Using the model of *Zhang et al.* [2003], *Chouet et al.* [2006] show that a drop in water concentration from just 1 weight percent to 0 will result in an increase in viscosity from 10^7 to 10^{11} Pa s in a rhyolite at 850°C. The less silicic, and therefore less viscous, Mount St. Helens dacite must behave similarly. So, while the spines appear solid at the surface, they are likely to be viscous enough to deform at rates modeled from the VLP data at shallow depth.

[96] We can speculate about other possible mechanisms for the VLP signals as well. For example, rather than assuming steady rates of degassing and crystallization within the conduit, a rapid change in pressure within the conduit could temporarily increase the rate of degassing and crystallization. Such a rapid pressure change could result from sag of the lava dome and spine implied by the LP mechanism. Increased gas exsolution could temporarily inflate the conduit, resulting in the VLP seismic signal we observe. As with the model presented earlier, in this model the VLP event results from a passive response of the magmatic system to the active LP mechanism.

[97] Unfortunately, the relative timing of the VLP and LP earthquakes is difficult to determine due to the difference in frequencies of the events and their emergent onsets. Various filtering techniques could not isolate the VLP onset precisely. In Figure 10, we see the beginning of the VLP signal before the broadband LP event on some channels. However, this precursory signal has a longer period than our 30-s instruments can faithfully record. In fact, the main part of the VLP signal occurs after the initiation of the LP event. This is clear when looking at the broadband displacement records in Figure 10b. Our recording capability is limited to seismic velocities with periods less than about 40 s, so longer-period signals that may precede the observed VLP are undetected. Tiltmeters installed on the 1980s dome show a variety of signals with periods in excess of 10 min. We

cannot directly relate these to the observed VLP signals since the recording periods do not overlap. However, the analysis of some tilt signals observed in the spring of 2006 indicates a source beneath the 1980s lava dome (M. Lisowski, personal communication, 2006–2007), very close to the epicenter of the VLP source.

5. Conclusions

[98]   Our analysis of broadband recordings made at Mount St. Helens in summer 2005 images the sources of VLP and a majority subset of drumbeat earthquakes. Rather than stick-slip motion along the magma conduit wall, we find that the source is dominated by a resonating, subhorizontal, north-dipping, steam-filled crack that underlies the growing lava dome. These drumbeat earthquakes are LP events. When they are distinguishable, only dilatational first motions are observed on the broadband stations, consistent with collapse of the crack. Crack resonance apparently initiates with partial crack closure. Oscillations of this crack are linked to movement of the lava spine and overlying dome, which produces a nearly vertical reaction force on the Earth. Waveform similarity for a majority of the LP earthquakes recorded between mid June and early September 2005 suggests that this mechanism is relatively stable for months. We do find a westward migration of the LP source centroid during July that can be explained by a change in the dome center of mass, but we propose that the LP crack source has been active for much longer than our two-month study period.

[99]   The LP source is linked to the source of VLP events and we view it as the causal event triggering a transient disruption of the otherwise smooth lava extrusion. Waveform inversion of the VLP events reveals a north-dipping sill plus a near-vertical dike or pipe. The VLP source sill is roughly in the plane of the LP source crack; it is deeper and to the north beneath the 1980s lava dome. The main VLP signal is generated by the deflation-inflation of the sill and near-simultaneous inflation-deflation of the dike. Large, subhorizontal forces that accompany the crack volume changes are interpreted as reaction forces on the Earth resulting from transient mass advection in the conduit. Exsolved magmatic gasses, primarily water, combined with groundwater vaporized by the heat of the magma, are the likely fluids filling the LP crack. The continuous supply of heat and fluid from the magmatic system is necessary to keep the crack pressurized and the drumbeats beating.

References

Akaike, H. (1974), A new look at the statistical model identification, *IEEE Trans. Auto. Control*, *19*, 716–723.

Aki, K. (1984), Evidence for magma intrusion during the Mammoth Lakes earthquakes of May 1980 and implications of the absence of volcanic (harmonic) tremor, *J. Geophys. Res.*, *89*, 7689–7696.

Aki, K., and P. G. Richards (1980), *Quantitative Seismology*, Freeman, New York.

Almendros, J., B. Chouet, P. B. Dawson, and T. Bond (2002), Identifying elements of the plumbing system beneath Kilauea Volcano, Hawaii, from the source locations of very-long-period signals, *Geophys. J. Int.*, *148*, 303–312.

Arciniega-Ceballos, A., B. A. Chouet, and P. Dawson (1999), Very long-period signals associated with vulcanian explosions at Popocatépetl volcano, Mexico, *Geophys. Res. Lett.*, *26*, 3013–3016, doi:10.1029/1999GL005390.

Aster, R., S. Mah, P. Kyle, W. McIntosh, N. Dunbar, J. Johnson, M. Ruiz, and S. McNamara (2003), Very long period oscillations of Mount Erebus Volcano, *J. Geophys. Res.*, *108*(B11), 2522, doi:10.1029/2002JB002101.

Auger, E., L. D'Auria, M. Martini, B. Chouet, and P. Dawson (2006), Real-time monitoring and massive inversion of source parameters of very long period seismic signals: An application to Stromboli Volcano, Italy, *Geophys. Res. Lett.*, *33*, L04301, doi:10.1029/2005GL024703.

Burlini, L., S. Vinciguerra, G. Di Toro, G. De Natale, P. Meredith, and J.-P. Burg (2007), Seismicity preceding volcanic eruptions: New experimental insights, *Geology*, 183–186, doi:10.1130/G23195A.1.

Cashman, K. V., C. R. Thornber, and J. S. Pallister (2008), From dome to dust: shallow crystallization and fragmentation of conduit magma during the 2004-2006 dome extrusion of Mount St. Helens, Washington, in *A Volcano rekindled: the first year of renewed eruptions at Mount St. Helens, 2004-2006*, edited by D. R. Sherrod, W. E. Scott, and P. H. Stauffer, *U.S. Geolog. Surv. Prof. Pap.*, *1750*, in press.

Chouet, B. (1981), Ground motion in the near field of a fluid-driven crack and its interpretation in the study of shallow volcanic tremor, *J. Geophys. Res.*, *86*, 5985–6016.

Chouet, B. (1988), Resonance of a fluid-driven crack: Radiation properties and implications for the source of long-period events and harmonic tremor, *J. Geophys. Res.*, *93*, 4347–4400.

Chouet, B. (1992), A seismic model for the source of long-period events and harmonic tremor, in *IAVCEI Proceedings in Volcanology 3*, edited by P. Gasparini, R. Scarpa, and K. Aki, pp. 133–156.

Chouet, B. A. (1996a), Long-period volcano seismicity: Its source an use in eruption forecasting, *Nature*, *380*, 309–316, doi:10.1038/380309a0.

Chouet, B. A. (1996b), New Methods and Future Trends in Seismological Volcano Monitoring, in *Monitoring and Mitigation of Volcano Hazards*, edited by R. Scarpa and R. I. Tilling, pp. 23–97, Springer-Verlag, Berlin.

Chouet, B., P. Dawson, T. Ohminato, M. Martini, G. Saccorotti, F. Giudicepietro, G. D. Luca, G. Milana, and R. Scarpa (2003), Source mechanisms of explosions at Stromboli Volcano, Italy, determined from moment-tensor inversions of very-long-period data, *J. Geophys. Res.*, *108*(B1), 2019, doi:10.1029/2002JB001919.

Chouet, B., P. Dawson, and A. Arciniega-Ceballos (2005), Source mechanism of Vulcanian degassing at Popocatépetl Volcano, Mexico, determined from waveform inversions of very long period signals, *J. Geophys. Res.*, *110*, B07301, doi:10.1029/2004JB003524.

Chouet, B., P. Dawson, and M. Nakano (2006), Dynamics of diffusive bubble growth and pressure recovery in a bubbly rhyolitic melt embedded in an elastic solid, *J. Geophys. Res.*, *111*, B07310, doi:10.1029/2005JB004174.

Dzurisin, D., J. W. Vallance, T. M. Gerlach, S. C. Moran, and S. D. Malone (2005), Mount St. Helens reawakens, *Eos Trans. AGU*, *86*, 25, 29, doi:10.1029/2005EO030001.

Ferrazzini, V., and K. Aki (1987), Slow waves trapped in a fluid-filled infinite crack: Implication for volcanic tremor, *J. Geophys. Res.*, *92*, 9215–9224.

Gerlach, T. M., K. A. McGee, and M. P. Doukas (2008), Emission Rates of CO_2, SO_2, and H_2S, Scrubbing, and Preeruption Excess Volatiles at Mount St. Helens, 2004-2005, in *A Volcano rekindled: the first year of renewed eruptions at Mount St. Helens, 2004-2006*, edited by D. R. Sherrod, W. E. Scott, and P. H. Stauffer, *U.S. Geolog. Surv. Prof. Pap.*, *1750*, in press.

Harrington, R. M., and E. E. Brodsky (2007), Volcanic hybrid earthquakes that are brittle-failure events, *Geophys. Res. Lett.*, *34*, L06308, doi:10.1029/2006GL028714.

Hidayat, D., B. Voight, B. Chouet, P. Dawson, and A. Ratdomopurbo (2002), Source mechanism of very-long-period signals accompanying dome growth activity at Merapi volcano, Indonesia, *Geophys. Res. Lett*, *29*, 1–33.

Hill, D. P., P. Dawson, M. J. S. Johnston, A. M. Pitt, G. Biasi, and K. Smith (2002), Very-long-period volcanic earthquakes beneath Mammoth Mountain, California, *Geophys. Res. Lett.*, *29*(10), 1370, doi:10.1029/2002GL014833.

Iverson, R. M. (2008), Dynamics of Seismogenic Volcanic Extrusion Resisted by a Solid Surface Plug, Mount St. Helens, 2004-2005, in *A Volcano rekindled: the first year of renewed eruptions at Mount St.*

Helens, 2004-2006, edited by D. R. Sherrod, W. E. Scott, and P. H. Stauffer, *U.S. Geolog. Surv. Prof. Pap.*, *1750*, in press.

Iverson, R. M., et al. (2006), Dynamics of seismogenic volcanic extrusion at Mount St. Helens in 2004-05, *Nature*, *444*, 439–443, doi:10.1038/nature05322.

James, M. R., S. J. Lane, and B. A. Chouet (2006), Gas slug ascent through changes in conduit diameter: Laboratory insights into a volcano-seismic source process in low-viscosity magmas, *J. Geophys. Res.*, *111*, B05201, doi:10.1029/2005JB003718.

Kanamori, H., and J. W. Given (1982), Analysis of long-period seismic waves excited by the May 18, 1980, eruption of Mount St. Helens - A terrestrial monopole, *J. Geophys. Res.*, *87*, 5422–5432.

Kaneshima, S., et al. (1996), Mechanism of phreatic eruptions at Aso volcano inferred from near-field broadband seismic observations, *Science*, *273*, 642–645.

Kawakatsu, H., T. Ohminato, H. Ito, and Y. Kuwahara (1992), Broadband seismic observation at the Sakurajima volcano, Japan, *Geophys. Res. Lett.*, *19*, 1959–1962.

Kawakatsu, H., T. Ohminato, and H. Ito (1994), 10s-period volcanic tremors observed over a wide area in southwestern Japan, *Geophys. Res. Lett.*, *21*, 1963–1966, doi:10.1029/94GL01683.

Kumagai, H., and B. A. Chouet (2000), Acoustic properties of a crack containing magmatic or hydrothermal fluids, *J. Geophys. Res.*, *105*, 25,493–25,512, doi:10.1029/2000JB900273.

Kumagai, H., T. Ohminato, M. Nakano, M. Ooi, A. Kubo, H. Inoue, and J. Oikawa (2001), Very-long-period seismic signals and caldera formation at Miyake Island, Japan, *Science*, *293*, 687–690, doi:10.1126/science.1062136.

Kumagai, H., B. A. Chouet, and M. Nakano (2002), Waveform inversion of oscillatory signatures in long-period events beneath volcanoes, *J. Geophys. Res.*, *107*(B11), 2301, doi:10.1029/2001JB001704.

Kumagai, H., B. A. Chouet, and P. B. Dawson (2005), Source process of a long-period event at Kilauea volcano, Hawaii, *Geophys. J. Int.*, *161*, 243–254, doi:10.1111/j.1365246X.2005.02502.x.

Kumazawa, M., Y. Imanishi, Y. Fukao, M. Furumoto, and A. Yamamoto (1990), A theory of spectral analysis based on the characteristic property of a linear dynamic system, *Geophys. J. Int.*, *101*, 613–630, doi:10.1111/j.1365-246X.1990.tb05574.x.

Legrand, D., S. Kaneshima, and H. Kawakatsu (2000), Moment tensor analysis of near-field broadband waveforms observed at Aso volcano, Japan, *J. Volcanol. Geotherm. Res.*, *101*, 155–169, doi:10.1016/S0377-0273(00)00167-0.

Matoza, R. S., M. A. H. Hedlin, and M. A. Garces (2007), An infrasound array study of Mount St. Helens, *J. Volcanol. Geotherm. Res.*, *160*, 249–262, doi:10.1016/j.jvolgeores.2006.10.006.

McNutt, S. R. (2005), Volcanic Seismology, *Annu. Rev. Earth Planet. Sci.*, *32*, 461–491, doi:10.1146/annurev.earth.33.092203.122459.

Moran, S. C., S. D. Malone, A. I. Qamar, W. Thelen, A. K. Wright, and J. Caplan-Auerback (2008), 2004-2005 seismicity associated with the renewed dome-building eruption of Mount St. Helens, in *A Volcano rekindled: the first year of renewed eruptions at Mount St. Helens, 2004-2006*, edited by D. R. Sherrod, W. E. Scott, and P. H. Stauffer, *U.S. Geolog. Surv. Prof. Pap.*, *1750*, in press.

Murase, T., and A. R. McBirney (1973), Properties of some common igneous rocks and their melts at high temperatures, *Geol. Soc. Am. Bull.*, *84*, 3563–3592.

Nakano, M., H. Kumagai, B. Chouet, and P. Dawson (2007), Waveform inversion of volcano-seismic signals for an extended source, *J. Geophys. Res.*, *112*, B02306, doi:10.1029/2006JB004490.

Nettles, M., and G. Ekström (1998), Faulting mechanism of anomalous earthquakes near Bárdarbunga Volcano, Iceland, *J. Geophys. Res.*, *103*, 17,973–17,984, doi:10.1029/98JB01392.

Neuberg, J., and T. Pointer (2000), Effects of volcano topography on seismic broad band waveforms, *Geophys. J. Int.*, *143*, 239–248, doi:10.1046/j.1365-246x.2000.00251.x.

Neuberg, J., R. Luckett, M. Ripepe, and T. Braun (1994), Highlights from a seismic broadband array on Stromboli Volcano, *Geophys. Res. Lett.*, *21*, 749–752, doi:10.1029/94GL00377.

Nishimura, T., T. Kobayashi, M. Ohtake, H. Sato, H. Nakamichi, S. Tanaka, M. Sato, S. Ueki, and H. Hamaguchi (2000), Source process of very long period seismic events associated with the 1998 activity of Iwate Volcano, northeastern Japan, *J. Geophys. Res.*, *105*, 19,135–19,147, doi:10.1029/2000JB900155.

Ohminato, T., and B. A. Chouet (1997), A free-surface boundary condition for including 3D topography in the finite-difference method, *Bull. Seismol. Soc. Am.*, *87*, 494–515.

Ohminato, T., B. A. Chouet, P. Dawson, and S. Kedar (1998), Waveform inversion of very long period impulsive signals associated with magmatic injection beneath Kilauea Volcano, *J. Geophys. Res.*, *103*, 23,839–23,862, doi:10.1029/98JB01122.

Onizawa, S., H. Mikada, H. Watanabe, and S. Sakashita (2002), A method for simultaneous velocity and density inversion and its application to exploration of subsurface structure beneath Izu-Oshima volcano, Japan, *Earth Planets Space*, *54*, 803–817.

Pallister, J. S., C. R. Thornber, K. V. Cashman, M. A. Clynne, H. A. Lowers, C. W. Mandeville, I. K. Brownfield, and G. P. Meeker (2008), Petrology of the 2004-2006 Mount St. Helens lava dome-implications for magmatic plumbing and eruption triggering, in *A Volcano rekindled: the first year of renewed eruptions at Mount St. Helens, 2004-2006*, edited by D. R. Sherrod, W. E. Scott, and P. H. Stauffer, *U.S. Geolog. Surv. Prof. Pap.*, *1750*, in press.

Poland, M. P., D. Dzurisin, R. G. LaHusen, J. J. Major, D. Lapcewich, E. T. Endo, D. J. Gooding, S. P. Schilling, and C. G. Janda (2008), Remote camera observations of lava dome growth at Mount St. Helens, Washington, October 2004-February 2006, in *A Volcano rekindled: the first year of renewed eruptions at Mount St. Helens, 2004-2006*, edited by D. R. Sherrod, W. E. Scott, and P. H. Stauffer, *U.S. Geolog. Surv. Prof. Pap.*, *1750*, in press.

Rowe, C. A., R. C. Aster, P. R. Kyle, R. R. Dibble, and J. W. Schlue (2000), Seismic and acoustic observations at Mount Erebus Volcano, Ross Island, Antarctica, 1994-1998, *J. Volcanol. Geotherm. Res.*, *101*, 105–128, doi:10.1016/S0377-0273(00)00170-0.

Scheu, B., H. Kern, O. Spieler, and D. B. Dingwell (2006), Temperature dependence of elastic P- and S-wave velocities in porous Mt. Unzen dacite, *J. Volcanol. Geotherm. Res.*, *153*, 136–147, doi:10.1016/j.jvolgeores.2005.08.007.

Schilling, S. P., R. A. Thompson, J. A. Messerich, and E. Y. Iwatsubo (2008), Use of Digital Aerophotogrammetry to Determine Rates of Lava Dome Growth, Mount St. Helens, 2004-2005, in *A Volcano rekindled: the first year of renewed eruptions at Mount St. Helens, 2004-2006*, edited by D. R. Sherrod, W. E. Scott, and P. H. Stauffer, *U.S. Geolog. Surv. Prof. Pap.*, *1750*, in press.

Scott, W. E., D. R. Sherrod, and C. A. Gardner (2008), Overview of 2004 to 2005, and Continuing, Eruption of Mount St. Helens, Washington, in *A Volcano rekindled: the first year of renewed eruptions at Mount St. Helens, 2004-2006*, edited by D. R. Sherrod, W. E. Scott, and P. H. Stauffer, *U.S. Geolog. Surv. Prof. Pap., 1750*, in press.

Takei, Y., and M. Kumazawa (1994), Why have the single force and torque been excluded from seismic source models?, *Geophys. J. Int.*, *118*, 20–30, doi:10.1111/j.1365-246X.1994.tb04672.x.

Thelen, W. A., R. S. Crosson, and K. C. Creager (2008), Absolute and Relative Locations of Earthquakes at Mount St. Helens, Washington Using Continuous Data: Implications for Magmatic Processes, in *A Volcano rekindled: the first year of renewed eruptions at Mount St. Helens, 2004-2006*, edited by D. R. Sherrod, W. E. Scott, and P. H. Stauffer, *U.S. Geolog. Surv. Prof. Pap.*, *1750*, in press.

Thelen, W., S. D. Malone, and S. C. Moran (2007), High or low? Frequency Games at Mount St. Helens, *Seism. Res. Lett.*, *78*, Ann. Meet. Abstract, 255.

Tuffen, H., and D. Dingwell (2005), Fault textures in volcanic conduits: evidence for seismic trigger mechanisms during silicic eruptions, *Bull. Volcanol.*, *67*, 370–387, doi:10.1007/s00445-004-0383-5.

Vallance, J. W., D. W. Schneider, and S. P. Schilling (2008), Growth of the 2004–2006 dome complex at Mount St. Helens, in *A Volcano rekindled: the first year of renewed eruptions at Mount St. Helens, 2004-2006*, edited by D. R. Sherrod, W. E. Scott, and P. H. Stauffer, *U.S. Geolog. Surv. Prof. Pap.*, *1750*, in press.

Waite, G. P., and S. C. Moran (2006), Crustal P-wave speed structure under Mount St. Helens from local earthquake tomography, *Eos Trans. AGU*, *87*, Fall Meet. Suppl., Abstract V11B-0578.

Zhang, Y., Z. Xu, and Y. Liu (2003), Viscosity of hydrous rhyolitic melts inferred from kinetic experiments, and a new viscosity model, *Am. Mineral.*, *88*, 1741–1752.

————————————

B. A. Chouet and P. B. Dawson, U.S. Geological Survey, Volcano Hazards, 345 Middlefield Rd., MS-910, Menlo Park, CA 94025, USA.

G. P. Waite, Geol. & Mining Eng. & Sci., Michigan Technological University, 1400 Townsend Dr, Houghton, MI 49931, USA. (gpwaite@mtu.edu; gwaite@usgs.gov)